P-ISSN 0126-3188
E-ISSN 2443-3926

BRIN
BADAN RISET
DAN INOVASI NASIONAL

METALURGI

VOLUME 38 No 1 2023

SCIENTIFIC JOURNAL ACCREDITATION NO.3/E/KPT/2019

National Research and Innovation Agency

METALURGI

VOLUME 38 NUMBER 1, 2023

P-ISSN 0126-3188
E-ISSN 2443-3926

ACCREDITATION : SK No. 3/E/KPT/2019

Publisher :
National Research and Innovation Agency (BRIN)
KST B.J. Habibie Serpong, Tangerang Selatan, Banten, Indonesia, 15314

E-mail: jurnalmetalurgi@mail.lipi.go.id

Science and technology magazine, regularly published every year; one volume consists of 3 editions

PREFACE

The author gives thanks to Allah for bestowing His blessing and direction, allowing the **Metalurgi Journal Volume 38, Edition 1**, **2023** to be successfully published.

The first article results from Ressa Muhripah Novianti and colleagues research activities on *The Addition of C, Zn-C, and Sn-C on Anatase Titanium Dioxide (TiO_2) for Dye-Sensitized Solar Cells Application*. Norbert Egan Christo Panthoko and his colleagues presented the second article, *Synthesis of Tin Oxide Nanocrystallites with Various Calcination Temperatures using Co-Precipitation Method with Local Tin Chloride Precursor*. Lalu Suhaimi and his colleagues presented *Recovery of Manganese from Manganese Ore Reductive Acid Leaching Process using Reeds (Imperata Cylindrica) as Reducing Agent* in the following article. For the fourth article, Rizky Ramadhani Rivai and his colleagues discussed *Characterization and Analysis of Hardness, Microstructure, and Crystallography of SS 304-Sheathed MgB_2 Superconducting Wires*. The fifth article, written by Arief Dwi Rohman and his colleagues, discussed *A Preliminary Study of Cobalt Solvent Extraction from Nickel Sulphate Solution using Organic Extractant PC-88A*.

The publication of this volume in Metalurgi Journal will benefit the advancement of research in Indonesia.

EDITORIAL

METALURGI

ISSN 0126 – 3188 Vol. 38, No. 1, 2023

Keywords sourced from articles. This abstract is reproduced without permission or fee.

UDC (OXDCF) 621.312

Ressa Muhripah Novianti[a], Natalita Maulani Nursam[b], Shobih[b], Jojo Hidayat[b], Syoni Soepriyanto[a] ([a]Department of Metallurgical Engineering, Bandung Institute of Technology, [b]Research Center for Electronics, National Research and Innovation Agency)

Metalurgi, Vol. 38, No. 1, 2023

The Addition of C, Zn-C, and Sn-C on Anatase Titanium Dioxide (TiO_2) for Dye-Sensitized Solar Cells Application

DSSC (dye-sensitized solar cell) is a third-generation photovoltaic technology that can convert solar energy into electric current using a photoelectrochemical mechanism. Photoelectrode is one of the significant elements in DSSC, where photoexcited electrons are generated, and serves as an electron transport medium. Anatase titanium dioxide (TiO_2) is often used as photoelectrode material because of its excellent photoactivity, high stability, non-toxicity, environmental friendliness, and low price. Many DSSC modifications have been conducted to overcome the efficiency limitations in DSSC, and one of them is carried out by modifying the TiO_2 via doping. In this study, TiO_2 doped with C and co-doping with Zn (Zn-C) and Sn (Sn-C) were prepared using sol-gel reactions, and they were subsequently applied and tested as photoelectrode in DSSC. The results showed that undoped and doped TiO_2 had a porous spherical morphology with inhomogeneous particle sizes. The addition of C, Zn-C and Sn-C dopants has reduced in the crystallite size and the band gap energy of TiO_2. The efficiency of DSSC with undoped TiO_2 DSSC was 3.83%, while the best performance was obtained from DSSC C-TiO_2 with an efficiency of 4.20%. In contrast, the DSSC with Zn-C-TiO_2 and Sn-C-TiO_2 co-doping produced unexpectedly lower efficiency of 0.71% and 0.85%, respectively.

Keywords: DSSC (dye-sensitized solar cell), TiO_2, photoelectrode, dopant, efficiency

METALURGI

ISSN 0126 – 3188 Vol. 38, No. 1, 2023

Keywords sourced from articles. This abstract is reproduced without permission or fee.

UDC (OXDCF) 669.6

Norbert Egan Christo Panthoko[a], Fairuz Septiningrum[a], Akhmad Herman Yuwono[a], Eka Nurhidayah[a], Fakhri Akbar Maulana[a], Nofrijon Sofyan[a], Donanta Dhaneswara[a], Tri Arini[b], Lia Andriyah[b], Florentinus Firdiyono[b], Latifa Hanum Lalasari[b], Yahya Winda Ardianto[c], Ria Wardhani Pawan[c] ([a]Department of Metallurgical and Materials Engineering, University of Indonesia, [b]Research Center for Metallurgy, National Research and Innovation Agency, [c]PT Timah Industri)

Metalurgi, Vol. 38, No. 1, 2023

Synthesis of Tin Oxide Nanocrystallites with Various Calcination Temperatures using Co-Precipitation Method with Local Tin Chloride Precursor

Indonesia is one of the largest tin metal producers in the world, and one of its derivative products is tin chloride (SnCl4). This material has been used as a raw ingredient for the production of organotin compounds such as methyltin mercaptide for PVC (polyvinyl chloride) plastic industry as a heat stabilizer. On the other hand, this precursor can be used to synthesize SnO_2 nanomaterials, which have other strategic potentials, including photocatalysts and solar cell applications. In this study, the synthesis of SnO_2 nanocrystallites was carried out using a local tin chloride precursor via the co-precipitation method, followed by a calcination process at temperatures of 300, 400, 500, and 600 °C, for further usage as an ETL (electron transport layer) in a PSC (perovskite solar cell) device. The basic properties characterization was carried out using XRD (X-ray diffraction), ultraviolet-visible (UV-Vis) spectroscopy, and SEM (scanning electron microscopy), while the photocurrent-voltage (I-V) curve photovoltaic performance of the device was performed using a semiconductor parameter analyzer. The characterization results showed that increasing the calcination temperature from 300 to 600 °C increased the average crystallite size from 1.19 to 13.75 nm and decreased the band gap energy from 3.57 to 3.10 eV. The highest PCE (power conversion efficiency) was obtained from the device fabricated with SnO_2 nanocrystallites calcined at a temperature of 300 °C, which was 0.0024%. This result was obtained due to the highest transmittance of this sample as compared to others; the higher the transmittance, the better the performance of the ETL, which in turn increased the overall efficiency of the PSC.

Keywords: SnO_2 nancrystallites, co-precipitation method, calcination temperature, electron transport layer, perovskite solar cell

METALURGI

ISSN 0126 – 3188 Vol. 38, No. 1, 2023

Keywords sourced from articles. This abstract is reproduced without permission or fee.

UDC (OXDCF) 546.5

Lalu Suhaimi, Samsul Bahtiar, Andi Sarina, Khairunnisya (Metallurgical Engineering, Sumbawa University of Technology)

Metalurgi, Vol. 38, No. 1, 2023

Recovery of Manganese from Manganese Ore Reductive Acid Leaching Process using Reeds (Imperata Cylindrica) as Reducing Agent

Recovery of manganese from manganese ores was investigated by reductive leaching method using reeds as a reductant in the sulfuric acid medium. Cellulose, hemicellulose, and lignin are natural reducing agents which are widely used as reducing agents to recover manganese. Effects of calcination temperature and the holding time calcination on the leaching efficiency of manganese and impurities were examined. The calcination temperature and the holding time calcination have a significant effect on the extraction of manganese. The experimental results demonstrated that the higher the calcination temperature used, the higher the percentage of manganese obtained, namely 79.58% and 87.38%, respectively. The XRD (x-ray diffraction) pattern shows that the manganese phases formed at 700 and 800 °C are Mn_3O_4 (hausmannite) and Mn_2O_3 (bixbite), respectively. The morphology in the sample with calcination temperature at 700 °C showed agglomerate-shaped particles and unevenly dispersed. Meanwhile, the sample with calcination temperature at 800 °C exhibited agglomerated particles of inhomogeneous size and were more evenly distributed. Variation of holding time in the manganese ores recovery process also affects the results of manganese recovery. The composition of the manganese recovery in the samples using holding time calcination variations of 3 and 4 hours was 83.88% and 89.24%, respectively. The results of the XRD analysis showed that the manganese phase formed using 3 hours of calcination holding time was dominated by Mn_3O_4 (hausmannite). Meanwhile, the manganese phase formed using 4 hours of holding time of calcination was dominated by Mn_2O_3 (bixbite).

Keywords: Reeds, manganese, reductant, Mn_3O_4 (haussmannite), Mn_2O_3 (bixbite)

METALURGI

ISSN 0126 – 3188 Vol. 38, No. 1, 2023

Keywords sourced from articles. This abstract is reproduced without permission or fee.

UDC (OXDCF) 621.35

Rizky Ramadhani Rivai[1], Andika Widya Pramono[2], Tri Hardi Priyanto[3], Awan Maghfirah[1] ([1]Physics Study Program, Faculty of Mathematics and Natural Sciences, University of North Sumatra, [2]Research Center for Advanced Materials, [3]Research Center for Radiation Detection and Nuclear Analysis Technology, National Research and Innovation Agency)

Metalurgi, Vol. 38, No. 1, 2023

Characterization and Analysis of Hardness, Microstructure, and Crystallography of SS 304-Sheathed MgB_2 Superconducting Wires

This research was conducted to analyze the hardness, microstructural morphology, and crystallography of the MgB_2 compound in the form of a SS 304-sheathed superconducting wire. MgB_2 superconducting wire with SS 304 outer sheath was manufactured using an ex-situ rolling process. The results of the Vickers hardness test with a load of 0.3 N showed the MgB_2 hardness value of 355.1 HV. The results of observations with SEM-EDS (scanning electron microscopy-energy dispersive spectroscopy) showed the agglomerations of the second phase of (Mg)B-O with various compositions due to the rolling process. There was also a longitudinal crack in the MgB2 area due to the work-hardening phenomenon in the brittle MgB2 solid. There were no obvious Bragg peaks in the MgB2 phase. The detected Bragg peaks came from the austenitic (□-Fe) of SS 304-sheath.

Keywords: magnesium diboride, agglomeration, FCD/TD, crystallographic texture, neutron absorption

METALURGI

ISSN 0126 – 3188 Vol. 38, No. 1, 2023

Keywords sourced from articles. This abstract is reproduced without permission or fee.

UDC (OXDCF) 546.6

Arief Dwi Rohman[a], Rudi Subagja[b], Anistasia Milandia[a], Soesaptri Oediyani[a], Iwan Setiawan[b] ([a]Metallurgical Engineering, Sultan Ageng Tirtayasa University, [b]Research Centre for Metallurgy, National Research and Innovation Agency)

Metalurgi, Vol. 38, No. 1, 2023

A Preliminary Study of Cobalt Solvent Extraction from Nickel Sulphate Solution using Organic Extractant PC-88A

In the present study, a solvent extraction experiment was done to separate cobalt from the nickel sulfate solution using 2-ethylhexyl phosphonic acid mono-2-ethylhexyl ester (PC-88A) as an extractant. The experiment was carried out on a laboratory scale using a separating funnel to extract cobalt from the nickel sulfate solution with PC-88A. The mixed solution was shaken in a separating funnel for a specified time. After the solvent extraction experiment was finished, the organic phase PC-88 was separated from the nickel sulfate solution by decantation. The nickel and cobalt content in the aqueous nickel sulfate solution was then analyzed using AAS (atomic absorption spectrophotometry). In this experiment, the variable for experiments was covering solution pH from 2 to 6, shaking time from 30 minutes to 120 minutes, shaking speed from 20 rpm (revolutions per minute) to 80 rpm, and the volume ratio of aqueous to organic phase (A:O ratio) was from 1:1 to 1:4. The effects that experimental variables to the cobalt extraction were observed in this experiment. The result of the experiment at room temperature, solution pH 5, shaking speed 60 rpm, shaking time 90 minutes, A:O ratio 1:4 and concentration of PC- 88A 40% show PC-88A can extract 97.21% of cobalt from nickel sulfate solution. Therefore, it was necessary to conduct two stage extraction process to extract 100% of the cobalt from the nickel sulfate solution.

Keywords: Solvent extraction, nickel, cobalt, nickel sulphate, PC-88A

METALURGI
Majalah Ilmu dan Teknologi
p-ISSN 0126-3188 | e-ISSN 2443-3926
ejurnalmaterialmetalurgi.lipi.go.id

THE ADDITION OF C, Zn-C, AND Sn-C ON ANATASE TITANIUM DIOXIDE (TiO_2) FOR DYE-SENSITIZED SOLAR CELLS APPLICATION

Ressa Muhripah Novianti[a], Natalita Maulani Nursam[b,*], Shobih[b], Jojo Hidayat[b], Syoni Soepriyanto[a]

[a]Department of Metallurgical Engineering, Bandung Institute of Technology
Jl. Ganesa No.10, Bandung, Indonesia 40132
[b]Research Center for Electronics, National Research and Innovation Agency
KST Samaun Samadikun, Jl. Sangkuriang-Cisitu, Bandung, Indonesia 40135
*E-mail: natalita.maulani.nursam@brin.go.id

Received: 23-11-2022, Revised: 27-01-2023, Accepted: 28-03-2023

Abstract

DSSC (dye-sensitized solar cell) is a third-generation photovoltaic technology that can convert solar energy into electric current using a photoelectrochemical mechanism. Photoelectrode is one of the significant elements in DSSC, where photoexcited electrons are generated, and serves as an electron transport medium. Anatase titanium dioxide (TiO_2) is often used as photoelectrode material because of its excellent photoactivity, high stability, non-toxicity, environmental friendliness, and low price. Many DSSC modifications have been conducted to overcome the efficiency limitations in DSSC, and one of them is carried out by modifying the TiO_2 via doping. In this study, TiO_2 doped with C and co-doping with Zn (Zn-C) and Sn (Sn-C) were prepared using sol-gel reactions, and they were subsequently applied and tested as photoelectrode in DSSC. The results showed that undoped and doped TiO_2 had a porous spherical morphology with inhomogeneous particle sizes. The addition of C, Zn-C and Sn-C dopants has reduced in the crystallite size and the band gap energy of TiO_2. The efficiency of DSSC with undoped TiO_2 DSSC was 3.83%, while the best performance was obtained from DSSC C-TiO_2 with an efficiency of 4.20%. In contrast, the DSSC with Zn-C-TiO_2 and Sn-C-TiO_2 co-doping produced unexpectedly lower efficiency of 0.71% and 0.85%, respectively.

Keywords: *DSSC (dye-sensitized solar cell), TiO_2, photoelectrode, dopant, efficiency*

1. INTRODUCTION

The increasing human population increased demand for energy sources [1]. Most energy consumed globally comes from non-renewable sources, which will eventually deplete. In addition, using these energy sources can cause environmental pollution [2]. Therefore, it is necessary to have alternative energy sources that can solve this problem. Solar cell is a semiconductor-based device that can convert sunlight directly into electrical current using photovoltaic principles without producing harmful emissions [3]. DSSC (dye-sensitized solar cell) is an emerging technology based on hybrid organic-inorganic materials. Brian O'Regan and Michael Gratzel first discovered the solar cell in 1991. To name a few, DSSC offers the benefit of low production cost, a simple fabrication process, and abundant and environmentally friendly materials [4]-[5].

Photoelectrode is one of the essential elements that determine the performance of DSSC. The semiconductor layer in the photoelectrode acts as a medium to transfer electrons from the dye molecules to the conductive substrate [6]. Titanium dioxide (TiO_2) semiconductor is mostly used as photoelectrode material in DSSC because of its properties, such as excellent photoactivity, chemical stability, non-toxicity, environmental friendliness, and low price. Among the three TiO_2 phases, TiO_2 with an anatase phase is preferred due to its superior optical and physical properties [2].

During the past years, many efforts have been carried out to boost the power conversion efficiency of DSSC, one of which was done by

DOI : 10.55981/metalurgi.686

Metalurgi is Sinta 2 Journal (https://sinta.ristekbrin.go.id/journals/detail?id=3708) accredited by Ministry of Research & Technology, Republic Indonesia

modifying TiO_2 via doping. The choice of dopants for doping on TiO_2 was considered from several things, including the atomic radius. Zn and Sn atoms with atomic radii of 1.42 Å and 1.40 Å, respectively, are the two potential candidates to be substituted into the TiO_2 crystal lattice, replacing some Ti atoms with atomic radii of 1.47 Å. In addition, Zn and Sn also have good electrical properties, are resistant to corrosion, could increase the photoactivity of TiO_2, and could maintain the stability of the anatase TiO_2 phase structure [7]-[9]. In addition to metal dopants, doping using a non-metallic element, such as C atoms with atomic radii 0.7 Å, is also viable because the atomic radius is not much different from the O atom 0.6 Å, thus making it possible to replace the O atom with C atom. C atom also has high photoactivity, good stability, is easy to obtain, and has been reported to help reduce the rate of electron-hole pair recombination [10]-[11].

The doping of TiO_2 could be carried out using various methods, such as hydrothermal, solvothermal, electrospinning, spray pyrolysis, liquid-phase deposition, and the sol-gel method. Among those many methods, the sol-gel method is preferred by many researchers due to its simplicity, and it can be used to obtain nanoparticles with tuneable particle size and homogeneity [12]. In this contribution, we report using the sol-gel technique to synthesize of TiO_2 doped with C and co-doped with Zn (Zn-C) and Sn (Sn-C). This work aims to analyze the effect of such TiO_2 photoanode modifications on the electrical performance of DSSC.

2. MATERIALS AND METHODS

2.1 Materials and Characterizations

The materials used are TTIP (titanium-IV isopropoxide), IPA (isopropyl alcohol), deionized water, aniline, $SnCl_2$ (solid crystalline tin-II chloride), $ZnCl_2$ (zinc chloride), FTO (fluorine-doped tin oxide) substrate, platinum paste, ruthenium dye (Z907), $TiCl_4$ solution, colloidal TiO_2, terpineol, triton, and EL-HPE electrolyte solution.

XRD (x-ray diffraction), SEM-EDX (scanning electron microscope-energy dispersive x-ray spectroscopy), and ultraviolet-visible diffusion reflectance spectroscopy (UV-vis DRS) measurements were conducted to characterize the physical and optical properties of the materials. Meanwhile, current-voltage (I-V) curves and IPCE (incident photon-to-current conversion efficiency) spectra were measured to analyze the resulting DSSC's electrical performance. The I-V characteristics were measured under a solar simulator (Newport) with a light intensity of 500 W/m^2 integrated with an AM1.5G filter.

2.2 Synthesis of Undoped TiO_2 and C-doped TiO_2

The synthesis was initiated by mixing 100 mL of IPA with 10 mL of deionized water and stirring with a magnetic stirrer for 30 min. Then, 1.56 mL of TTIP was added to the solution by dripping slowly using a pipette. For the synthesis of C-doped TiO_2 powder, 100 µL of aniline was added to the solution while stirred for 4 h with a stirring speed of 6000 rpm. As for the synthesis of undoped TiO_2 powder, no aniline was added during the stirring. After stirring, the mixture was allowed to stand at room temperature for 72 hours until a gel precipitate was formed. The gel formed was then separated from the residue. After the gel was separated from the residue, the gel was dried in an oven at 70 °C for 6 h until a solid was formed. The resulting solids of undoped TiO_2 and C-doped TiO_2 were crushed using a mortar until a fine powder was formed. Then, the undoped TiO_2 and C-doped TiO_2 powders were calcined at 450 °C for 3 hours in a vacuum furnace to form the anatase phase.

2.3 Synthesis Zn-C and Sn-C Co-doped TiO_2

Powders of Zn-C and Sn-C co-doped TiO_2 (i.e., with 10 mol % Sn and Zn) were synthesized by dissolving 0.17 g of solid $ZnCl_2$ or 0.24 g of $SnCl_2$ into 50 mL IPA and 10 mL deionized water (solution A). Solution A was stirred for 20 min using a magnetic stirrer. In another glass beaker, 1.56 mL of TTIP was added little by little to 100 mL of IPA and stirred for 30 min using a magnetic stirrer to form a homogeneous solution (solution B). During the stirring of solution B, solution A was slowly poured into solution B, and continued for 4 hours at a stirring speed of 6000 rpm. The following process is the same as the steps in the synthesizing the undoped TiO_2 and C-doped TiO_2 powders.

2.4 Preparation of Undoped TiO_2, C Doped, Zn-C and Sn-C Co-doped TiO_2 Paste

The undoped TiO_2, C-doped, Zn-C, and Sn-C co-doped TiO_2 powder were made into pastes to be attached to the FTO glass by the screen printing method. A colloidal TiO_2 was required to make the paste as a binder to the mixture. The synthesis of colloidal TiO_2 was carried out by mixing 75 mL of deionized water with 2 mL of IPA in a reflux reactor. Then, 12.5 mL of TTIP was added to the mixture by dripping slowly using a pipette while stirring with a magnetic stirrer. After mixing the solution, it was

continued by adding 0.6 mL of 65% nitric acid (HNO_3). Next, the reflux reactor was paired with a condenser, heated, and stirred on a hot plate at 80 °C for 8 hours. Upon completion, a white and slightly transparent colloidal TiO_2 solution was obtained.

To prepare the paste, 0.26 grams of TiO_2/C-TiO_2/Zn-C-TiO_2/Sn-C-TiO_2 powder was crushed with a mortar until a fine powder was produced, and 0.2 mL of colloidal TiO_2 was added and stirred evenly. Then 0.1 mL of terpineol and 0.2 mL of triton were added as a binder solution and stirred evenly until there were no lumps.

2.5 Preparation of Photoelectrodes

Before the coating step, the FTO substrate was coated with a blocking layer by immersing the FTO substrate with 40 mM $TiCl_4$ solution on a hot plate at 70 °C for 30 min. After that, the substrate was rinsed twice using deionized water and dried. The dried substrate was sintered using a muffle furnace at 500 °C for 30 min.

Then the FTO substrate was coated with TiO_2/C-TiO_2/Zn-C-TiO_2/Sn-C-TiO_2 paste using a screen printing method, where the coating was carried out 2 times. The printed FTO substrate will be leveled for 5 min, then dried in the oven at 120 °C for 10 min and sintered in a vacuum furnace at 500 °C for 30 min.

The paste-coated FTO substrate was immersed in $TiCl_4$ solution in the same way as before to produce a TiO_2 reflector layer that increased light absorption in the DSSC.

The following process is the immersion of the samples in Z907 dye solution. The solution was prepared by dissolving 20 mg of Z907 dye powder with 100 mL of ethanol. The immersion was carried out for 24 h at room temperature. After immersion, the substrate was rinsed with ethanol and dried using a hair dryer.

2.6 Preparation of Counter Electrodes

The FTO substrates that have been perforated for electrolyte filling were coated with the platinum paste using the screen printing method. The paste coating process was carried out 2 times and then, the substrate was annealed at 450 °C in a belt conveyor furnace.

2.7 Dye-Sensitized Solar Cell Assembly

The finished photoelectrode and counter electrode were attached with surlyn thermoplastic using a hot press at 125 °C for 40 s. After the two substrates were attached, the EL-HPE electrolyte solution was injected into the gap between the two substrates through the hole on the counter electrode. After the electrolyte solution was filled, the hole on the counter electrode was closed with surlyn thermoplastic and aluminum foil by soldering. The DSSC that had been completely constructed was then coated with conductive silver ink on the sides of the counter electrode and photoelectrode to increase the conductivity during electrical measurements.

3. Result and Discussion

3.1 Crystal Structure

The crystal structure and phase composition of TiO_2, C-TiO_2, Zn-C-TiO_2, and Sn-C-TiO_2 were studied by XRD (x-ray diffraction) analysis, and the results are shown in Fig. 1. It can be seen that the diffraction peaks are relatively sharp, indicating that all samples have good crystallinity. Phase identification was made by matching the measured diffraction peak position data with the JCPDS (joint committee for powder diffraction standard). The diffraction patterns of TiO_2, C-TiO_2, and Zn-C-TiO_2 showed diffraction peaks indicating a single phase, that is, anatase. The typical peak of anatase TiO_2 was found at 2θ (°) 25.3°; 37.8°; and 48.07°, which is the highest intensity peak compared to other anatase diffraction peaks. In Sn-C-TiO_2, apart from the diffraction peak of the anatase phase, one peak indicates the rutile phase at 2θ=27.06°. The anatase phase is typically favourable in DSSC (dye-sensitized solar cell) because it has excellent photoactivity compared to other phases, especially for solar cell applications. This is because the anatase phase has a wider active surface area so that the absorption of dyes will be more optimal and has implications for more photons that can be absorbed [7],[13].

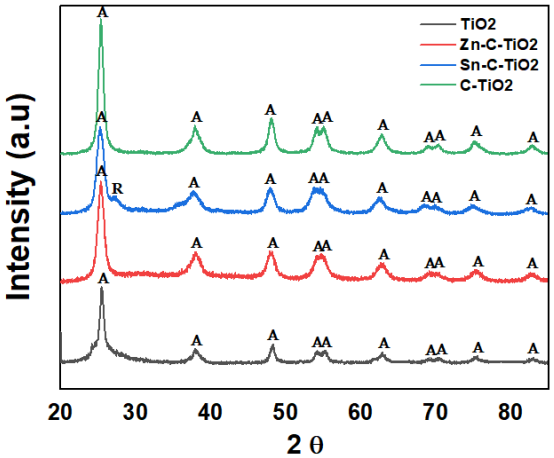

Figure 1. XRD patterns of undoped and various doped TiO_2

The presence of dopant atoms does not change the diffraction pattern. This indicates that the dopant Sn and Zn managed to enter the TiO_2 crystal lattice substituting the Ti atom, while C entered the crystal lattice substituting the O atom.

In addition, it is also seen that the presence of dopants indicates an increase in the intensity of the diffraction peak, suggesting enhanced crystallinity. With good crystallinity, the electron injection process in TiO_2 will be faster, and consequently, more photoexcited electrons could be transferred, which eventually will improve the performance of DSSC [7]-[8],[10],14].

The crystallite size was calcula[ted using the Debye-Scherrer equation as follows:

$$D = \frac{0{,}9\,\lambda}{\beta \cos\theta} \quad (1)$$

where λ is the x-ray wavelength (1.54 Å), β is the FWHM (full widht half maximum), and θ is the diffraction angle (degrees). The calculated crystallite sizes are shown in Table 1.

Table 1. Crystallite size of undoped and doped TiO_2

Samples	Anatase crystallite size (nm)	Rutile crystallite size (nm)	Crystallite size (nm)
TiO_2	87.26	-	87.26
C-TiO_2 1.5	80.49	-	80.49
Zn-C-TiO_2	53.67	-	53.67
Sn-C-TiO_2	56.43	57.65	57.04

The presence of C, Zn-C, and Sn-C dopant led to the formation of TiO_2 with smaller crystal size than that of the undoped TiO_2 due to a decrease in the regularity of the crystal lattice. This is because the presence of C, Zn, and Sn has been reported to slow down the growth of TiO_2 due to differences in atomic radius resulting in several degrees of lattice deformation [15].

3.2 Surface Analysis

The surface morphology of the undoped TiO_2 and doped TiO_2 semiconductors was analyzed using SEM, as shown in Fig. 2. The figure shows that the undoped TiO_2 and C-TiO_2 particles have irregular spherical shapes with inhomogeneous particle sizes. Similar morphology was also observed in Zn-C-TiO_2 and Sn-C-TiO_2, which exhibit inhomogeneous particle shapes and sizes. Many particle aggregates were also present, especially the TiO_2 samples with dopants. The inhomogeneous particle size distribution is likely to be caused by agglomeration. It can be seen that Zn-C-TiO_2 and Sn-C-TiO_2 contain more agglomerations than C-doped TiO_2, so the resulting particles seem relatively larger.

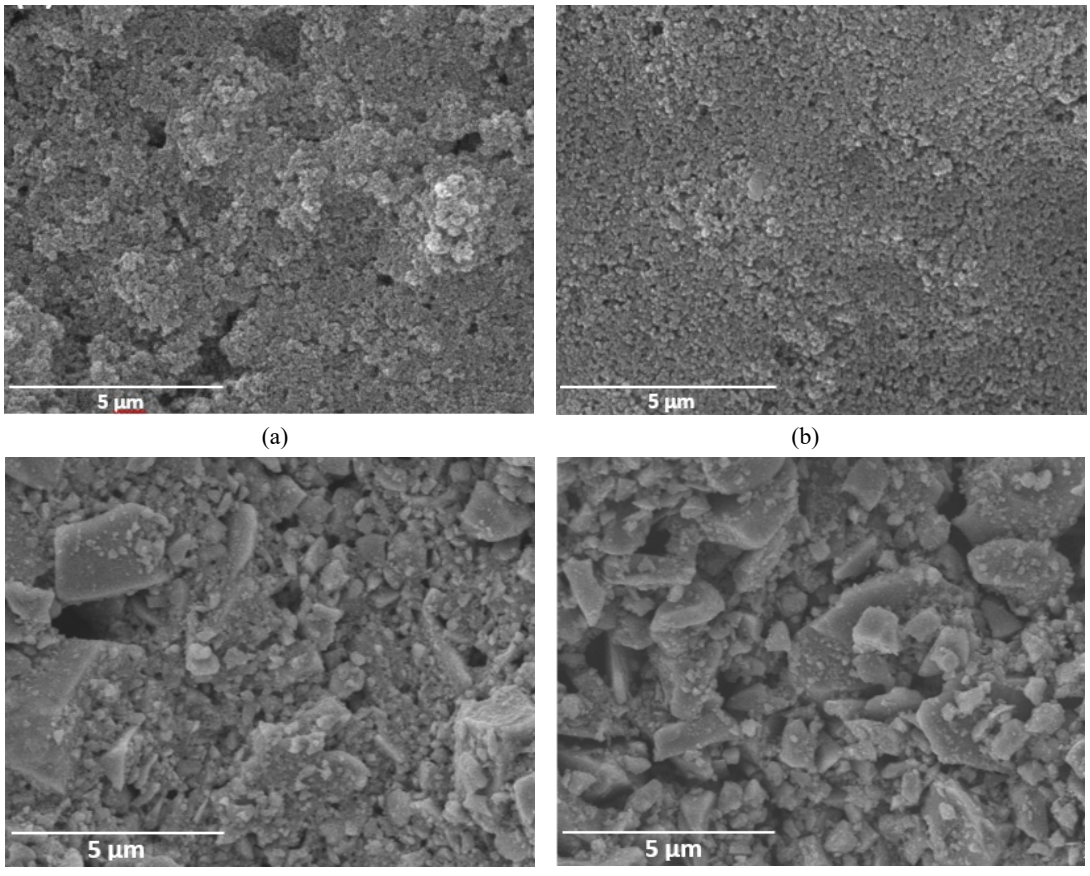

(a) (b) (c) (d)

Figure 2. Surface morphology of (a) TiO_2, (b) C-TiO_2, (c) Sn-C-TiO_2, and (d) Zn-C-TiO_2

In the morphology of the four samples, it can also be seen that some pores could facilitate the dye adsorption into the TiO_2 layer. Consequently, the number of photons that can be absorbed, as well as the redox pairs of the electrolyte, is expected to increase [16]. When more photons are absorbed, more electrons will be injected from the dyes into TiO_2, which will then be transported to the FTO substrate and the outer circuit to produce a higher photogenerated current.

EDX (energy dispersive x-ray spectroscopy) analysis was conducted to determine the elemental composition of undoped TiO_2 and doped TiO_2. The results of EDX are shown in Table 2. The content of elements produced from EDS shows the absence of other unexpected elements. In undoped TiO_2, C content is still obtained, almost the same as C-TiO_2 powder but in different amounts. The C content in undoped TiO_2 is thought to come from the TTIP (titanium-IV isopropoxide) precursor containing carbon and organic chains. Meanwhile, in the C-TiO_2 powder, the C content was attributed to the dopant precursor, aniline, and TTIP. Zn-C-TiO_2 has a minimal Zn element content of 0.59 %wt, while Sn-C-TiO_2 shows a reasonably high Sn element content of 18.16%wt. Dopant content that is too high is typically not expected because it can change the crystal properties of the TiO_2, as seen in the XRD (x-ray diffraction) Sn-C-TiO_2 diffraction pattern with the appearance of the rutile phase.

Table 2. Elemental composition of undoped and doped TiO_2

Sample	Wt (%)				
	Ti	O	C	Zn	Sn
TiO_2	48.46	46.47	5.06	-	-
C-TiO_2	48.44	45.85	5.70	-	-
Zn-C-TiO_2	53.96	41.53	3.92	0.59	-
Sn-C-TiO_2	35.88	41.08	4.88	-	18.16

3.3 UV-Vis DRS Analysis

The values of bandgap energy were calculated using the Kubelka-Munk equation from the measured UV-Vis DRS absorbance data:

$$F(R) = \frac{(1-R)^2}{2R} \quad (1)$$

where R is the reflectance. To estimate the bandgap value, a tangential line was fitted and extrapolated from the Kubelka-Munk absorbance data, and the results are shown in Table 3.

The bandgap energy of synthesized undoped TiO_2 is 3.03 eV, slightly lower than a typical bandgap energy value for anatase TiO_2, which is 3.2 eV. This is likely to be attributed to residual C content in the undoped TiO_2, as previously shown in the EDX results. The presence of this C content will form a new sub-band above the valence band so that it changes the band gap energy value.

The bandgap energy of Zn-C and Sn-C co-doped TiO_2 was 2.92 eV and 2.86 eV, respectively. The presence of Zn-C and Sn-C dopant atoms causes the bandgap energy to decrease due to the synergistic effect of the two dopant types, namely the formation of energy levels above the valence band and below the conduction band, which consequently increases the separation between holes and electrons [17]. These two new sub-bands are very beneficial for photocatalyst applications because the energy required for electron excitation from the valence band to the conduction band is getting smaller to increase the photocatalyst performance. It is different for DSSC applications. The presence of dopants will increase the absorption of the dye on TiO_2 and increase the energy for electron injection from the dye to TiO_2 [6]. This will have implications for the speed of electron transport from TiO_2 to the FTO substrate, followed by the flow of electrons to the external circuit for the current generation.

Table 3. Bandgap energy of undoped TiO_2 and doped TiO_2

Sample	Bandgap Energy (eV)
TiO_2	3.03
C-TiO_2	2.91
Zn-C-TiO_2	2.92
Sn-C-TiO_2	2.86

3.4 Photovoltaic Performance of DSSCs

To determine the performance of the DSSCs, an current-voltage (I-V) characterization test was carried out to obtain several important electrical parameters in the solar cell. These parameters are J_{SC} (short circuit current), V_{OC} (open circuit voltage), FF (fill factor), and power conversion efficiency (η), all of which are summarized in Table 4. The measurements were carried out under standardized solar cell characterization conditions, with irradiation from a solar simulator with an AM1.5G spectrum filter at room temperature.

The photocurrent density – voltage ($J - V$) curves measured on the fabricated DSSCs with various TiO_2 modifications are illustrated in Fig. 3. The value of *Voc, Jsc*, and FF are known to

DOI : 10.55981/metalurgi.686

Metalurgi is Sinta 2 Journal (https://sinta.ristekbrin.go.id/journals/detail?id=3708) accredited by Ministry of Research & Technology, Republic Indonesia

determine the efficiency of DSSC. From the *J-V* curves in Fig. 3 and the electrical parameters in Table 4, the undoped TiO_2 produced DSSC with *Jsc* of 4.24 mA/cm^2, *Voc* of 0.70 V, *FF* of 0.65, and efficiency of 3.83%. From the *J-V* curve, it can be seen that the DSSC with C-doped TiO_2 shows significantly better performance than the DSSC with Zn-C and Sn-C co-doped TiO_2. The DSSC parameters with C-doped TiO_2 produced a *Jsc* of 5.05 mA/cm^2, *Voc* of 0.67 V, *FF* of 0.62, and a power conversion efficiency of 4.21%.

Table 4. Electrical parameters of DSSC with photoelectrode variations

Sampel	Voc (V)	Jsc (mA/cm^2)	FF	Efficiency (%)
TiO_2	0.70	4.24	0.65	3.83
C-TiO_2	0.67	5.05	0.62	4.21
Zn-C-TiO_2	0.63	0.92	0.61	0.71
Sn-C-TiO_2	0.68	1.17	0.53	0.85

DSSC with Zn-C and Sn-C co-doped TiO_2 photoelectrodes produced lower DSSC parameters than the C-doped TiO_2 and even the undoped TiO_2. This indicates that the TiO_2 modifications for these two samples did not work as expected. It was observed that during the injection of electrolytes, the electrolyte solutions in Zn-C-TiO_2 and Sn-C-TiO_2 samples were challenging to be infiltrated into the cells.

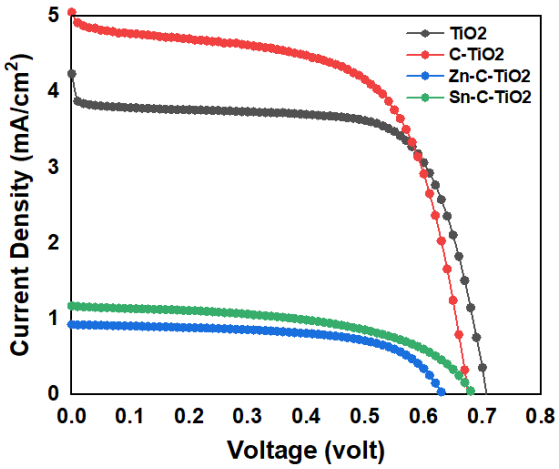

Figure 3. Photocurrent density-voltage curves of DSSCs with TiO_2 photoelectrode variations

The reason was possibly due to the hydrophobicity of the Zn-C-TiO_2 and Sn-C-TiO_2 surface properties [12]. Thus the wetting effect of the photoelectrode by the electrolyte took a lot of work to achieve. In turn, the performance of the DSSC will be affected because this electrolyte solution acts as a charge carrier that collects electrons at the counter electrode and brings electrons back to the dye molecule, resulting in an electron transfer cycle in the cell [19]. When there is insufficient electrolyte solution in the cell, the electron transfer cycle will be disrupted, thereby lowering the current generated by the DSSC.

In addition to the I-V test, IPCE (incident photon-to-current conversion efficiency) testing was also carried out to determine the spectral response of the DSSC. This test was carried out on selected samples that have previously shown high I-V performance for each variation.

Figure 4 shows the IPCE spectra that were collected between 300 to 800 nm. It can be seen that DSSC has a good photoelectric response in the UV light range of 300 – 370 nm and visible light range of 370 – 700 nm. The IPCE curves mainly consist of two absorption regions characterized by the presence of two light absorption peaks, i.e., the first peak was attributed to the light absorption by TiO_2. In contrast, the second peak was attributed to the light absorption by the dye molecules.

In the UV light region, the first peak is formed at a wavelength of 340 nm, which typically corresponds to the absorption band edge of TiO_2. Light absorption by TiO_2 occurs within the short-wave range because TiO_2 has a large band gap energy of around 3.0 – 3.2 eV, so higher energy is required for electron excitation. In the visible light region, the second peak at a wavelength of about 520 nm was mainly attributed to the light absorption by the ruthenium Z907 dyes [20]. The dye absorption that occurs in a longer wavelength range corresponds to the bandgap energy of dye at around ~1.5 eV. Hence the energy required for electron excitation is smaller than that required in TiO_2.

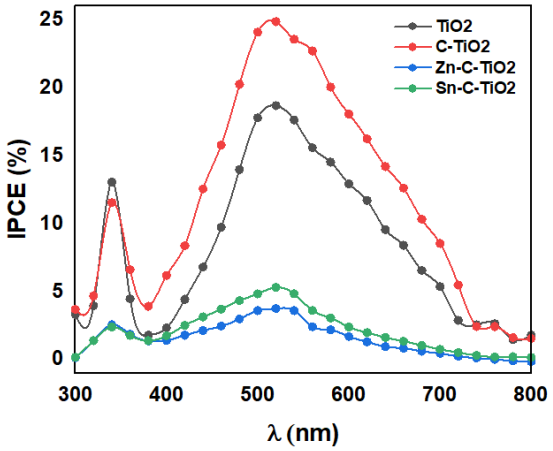

Figure 4. IPCE spectra of DSSCs with TiO_2 photoelectrode variations

The IPCE of DSSC values is determined by the amount of light that the dye can absorb, the number of electrons excited from the dye to the conduction band of TiO_2, and the number of photoexcited electrons transferred from the conduction band of TiO_2 to the external circuit. The highest IPCE value was shown by C-doped TiO_2, indicating that carbon is the most optimal dopant to improve the DSSC performance compared to Zn-C and Sn-C co-doped TiO_2. The higher IPCE value indicates that more photons are converted into the current [20]. The IPCE results align with the results obtained from the current-voltage measurement shown in Fig. 3, where the DSSC with C-doped TiO_2 photoelectrode produced the highest current density.

4. CONCLUSION

TiO_2 photoelectrodes modified with carbon doping and various co-doping were synthesized using a simple sol-gel method, and the resulting materials were applied and tested in DSSC (dye-sensitized solar cell). The presence of C, Zn, and Sn dopants overall decreased bandgap energy and crystal size. DSSC with C-doped TiO_2 achieved the highest performance with a power conversion efficiency of 4.21%. DSSC with co-doping modifications in the form of Zn-C-TiO_2 and Sn-C-TiO_2, produced lower efficiency than the DSSC with pristine TiO_2, which was suspected mainly due to poor wettability at the TiO_2/electrolyte interface.

ACKNOWLEDGMENT

The authors acknowledge support from Advanced PV and Functional Electronic Device research group at the Research Center for Electronics, National Research and Innovation Agency (BRIN) and, the Department of Metallurgical Engineering, Bandung Institute of Technology. E-Layanan Sains (ELSA) BRIN is gratefully acknowledged for access to the materials characterization facilities. This research project was partially funded by Riset dan Inovasi untuk Indonesia Maju or RIIM program by LPDP-BRIN (No. 65/II.7/HK/2022).

REFERENCES

[1] M. S. Ahmad, A. K. Pandey, and N. A. Rahim, "Advancements in the development of TiO_2 photoanodes and its fabrication methods for dye sensitized solar cell (DSSC) applications," *A review Renewable and Sustainable Energy Reviews*, vol. 77, pp. 89-108, 2017. Doi:10.1016/j.rser.2017. 03. 129.

[2] S. Zhuang, M. Lu, N. Zhou, L. Zhou, D. Lin, Z. Peng, and Q. Wu, "Cu modified ZnO nanoflowers as photoanode material for highly efficient dye sensitized solar cells," *Electrochimica Acta*, vol. 294, pp. 28-37, 2019. Doi:10.1016/j.electacta.2018.10.045.

[3] M. Khan, M. R. Al-Mamun, P. K. Halder, and M. A. Aziz, "Performance improvement of modified dye-sensitized solar cells," *Renewable and Sustainable Energy Reviews*, vol. 71, pp. 602-617, 2017. Doi:10.1016/j.rser.2016.12.087.

[4] R. S. Ganesh, K. Silambarasan, E. Durgadevi, M. Navaneethan, S. Ponnusamy, C. Y. Kong, C. Muthamizhchelvan, Y. Shimura, and Y. Hayakawa, "Metal sulfide nanosheet–nitrogen-doped graphene hybrids as low-cost counter electrodes for dye-sensitized solar cells," *Applied Surface Science*, vol. 480, pp. 177-185, 2019. Doi:10.1016/j.apsusc.2019.02.251.

[5] R. S. Ganesh, M. Navaneethan, S. Ponnusamy, C. Muthamizhchelvan, S. Kawasaki, Y. Shimura, and Y. Hayakawa, "Enhanced photon collection of high surface area carbonate-doped mesoporous TiO_2 nanospheres in dye sensitized solar cells," *Materials Research Bulletin*, vol. 101, pp. 353-362, 2018. Doi:10.1016/j.materresbull.2018. 01.018.

[6] L. Zhou, L. Wei, Y. Yang, X. Xia, P. Wang, J. Yu, and T. Luan, "Improved performance of dye sensitized solar cells using Cu-doped TiO_2 as photoanode materials : Band edge movement study by spectroelectrochemistry," *Chemical Physics*, vol. 475, pp. 1-8, 2016. Doi: 10.1016/j.chemphys. 2016.05.018.

[7] B. Li, and N. Tang, "Study on Zr, Sn, Pb, Si and Pt doped TiO_2 photoanode for dye-sensitized solar cells : The first-principles calculations," *Chemical Physics Letters*, vol. 799, pp. 139636, 2022. Doi:10.1016 /j.cplett. 2022.139636.

[8] S. Mehraz, P. Kongsong, A. Taleb, N. Dokhane, and L. Sikong, "Large scale and facile synthesis of Sn doped TiO_2 aggregates using hydrothermal synthesis," *Solar Energy Materials and Solar Cells*, vol. 189, pp. 254-262, 2019. Doi:10.1016/j.solmat.2017. 06.048.

[9] T. C. Paul, J. Podder, and M. H. Babu, "Optical constants and dispersion energy parameters of Zn-doped TiO_2 thin films prepared by spray pyrolysis technique," *Surfaces and Interfaces*, vol. 21, pp. 100725. Doi:10.1016/j.surfin.2020.100725.

[10] N. U. Nor, E. Mazalan, C. Risko, M. Crocker, and N. A. Amin, "Unveiling the structural, electronic, and optical effects of carbon-doping on multi-layer anatase TiO_2 (1 0 1) and the impact on photocatalysis," *Applied Surface Science*, vol. 586, pp. 152641, 2022. Doi:10.1016/j.apsusc.2022.152641.

[11] A. Colombo, C. Dragonetti, D. Roberto, R. Ugo, N. Manfredi, P. Manca, A. Abbotto, G. D. Giustina, and G. Brusatin, "A carbon doped anatase TiO_2 as a promising semiconducting layer in Ru-dyes based dye-sensitized solar cells," *Inorganica Chimica Acta,* vol. 489, pp. 263-268, 2019. Doi: 10.1016/j.ica.2019.02.024.

[12] O. Sadek, S. Touhtouh, M. Rkhis, R. Anoua, M. El Jouad, F. Belhora, and A. Hajjaji, "Synthesis by sol-gel method and characterization of nano-TiO_2 powders," *Materials Today : Proceedings*, 2022. Doi:10.1016/ j.matpr.2022.06.385.

[13] V. R. Gomez, I. M. D. L. Santos, D. S. Jiménez, F. A. Mató, A. Z. Lara, T. R. Bonilla, and M. Courel, "Recent advances in dye sensitized solar cells," *Advances in Materials Science and Engineering,* vol. 836, pp. 1-12, 2019. Doi:10.1007/s00339-019-3116-5.

[14] H. M. Javed, M. Adnan, A. A. Qureshi, S. Javed, M. Adeel, M. Shahid, and M. I. Ahmad, "Morphological, structural, thermal and optical properties of Zn/Mg-doped TiO_2 nanostructures for optoelectronics applications," *Optics & Laser Technology*, 146, pp. 107566, 2022. Doi: 10.1016/j.optlastec.2021.107566.

[15] H. Zhang, Z. Wu, R. Lin, and Y. Wang, "Exploring the mechanism of room temperature ferromagnetism in C-doped TiO_2 nanoclusters by tuning the defects by different annealing temperature using citric acid as C source," *Ceramics International*, vol. 48 (18), pp. 26836-26845, 2022. Doi: 10.1016/j.ceramint. 2022.05.385.

[16] E. M. Bayan, T. G. Lupeiko, L. E. Pustovaya, M. G.Volkova, V. V. Butova, and A. A. Guda, "Zn–F Co-doped TiO_2 nanomaterials: Synthesis, structure and photocatalytic activity," *Journal of Alloys and Compounds*, vol. 822, pp. 153662, 2020. Doi:10.1016/j.jallcom.2020.153662.

[17] S. Mehraz, P. Kongsong, A. Taleb, N. Dokhane, and L. Sikong, "Large scale and facile synthesis of Sn doped TiO_2 aggregates using hydrothermal synthesis," *Solar Energy Materials and Solar Cells*, vol. 189, pp. 254-262, 2020. Doi: 10.1016/j.solmat.2017. 06.048.

[18] S. Aghazada, and M. K. Nazeeruddin, "Ruthenium complexes as sensitizers in dye sensitized solar cells," *Inorganics*, vol. 6, pp. 1-34, 2018. Doi:10.3390/inorganics6020052.

[19] N. Shahzad, Lutfullah, T. Perveen, D. Pugliese, S. Haq, N. Fatima, S. M. Salman, A. Tagliaferro, and M. I. Shahzad, "Counter electrode materials based on carbon nanotubes for dye-sensitized solar cells," *Renewable and Suistanable Energy Reviews*, vol. 159, pp. 112196, 2022. Doi: 10.1016/j.rser.2022.112196.

Metalurgi (2023) 1: 9 - 18

METALURGI
Majalah Ilmu dan Teknologi
p-ISSN 0126-3188 | e-ISSN 2443-3926
ejurnalmaterialmetalurgi.lipi.go.id

SYNTHESIS OF TIN OXIDE NANOCRYSTALLITES WITH VARIOUS CALCINATION TEMPERATURES USING CO-PRECIPITATION METHOD WITH LOCAL TIN CHLORIDE PRECURSOR

Norbert Egan Christo Panthoko[a], Fairuz Septiningrum[a], Akhmad Herman Yuwono[a,*], Eka Nurhidayah[a], Fakhri Akbar Maulana[a], Nofrijon Sofyan[a], Donanta Dhaneswara[a], Tri Arini[b], Lia Andriyah[b], Florentinus Firdiyono[b], Latifa Hanum Lalasari[b], Yahya Winda Ardianto[c], Ria Wardhani Pawan[c]

[a]Department of Metallurgical and Materials Engineering, University of Indonesia
Kampus UI, Kukusan, Depok, Indonesia 16424
[b]Research Center for Metallurgy, National Research and Innovation Agency
B.J. Habibie Sains and Technology Area, Banten, Indonesia 15314
[c]PT Timah Industri
Industrial Estate Cilegon Area (KIEC), Banten, Indonesia 42435
*E-mail: ahyuwono@eng.ui.ac.id

Received: 30-11-2022, Revised: 03-04-2023, Accepted: 12-04-2023

Abstract

Indonesia is one of the largest tin metal producers in the world, and one of its derivative products is tin chloride ($SnCl_4$). This material has been used as a raw ingredient for the production of organotin compounds such as methyltin mercaptide for PVC (polyvinyl chloride) plastic industry as a heat stabilizer. On the other hand, this precursor can be used to synthesize SnO_2 nanomaterials, which have other strategic potentials, including photocatalysts and solar cell applications. In this study, the synthesis of SnO_2 nanocrystallites was carried out using a local tin chloride precursor via the co-precipitation method, followed by a calcination process at temperatures of 300, 400, 500, and 600 °C, for further usage as an ETL (electron transport layer) in a PSC (perovskite solar cell) device. The basic properties characterization was carried out using XRD (X-ray diffraction), ultraviolet-visible (UV-Vis) spectroscopy, and SEM (scanning electron microscopy), while the photocurrent-voltage (I-V) curve photovoltaic performance of the device was performed using a semiconductor parameter analyzer. The characterization results showed that increasing the calcination temperature from 300 to 600 °C increased the average crystallite size from 1.19 to 13.75 nm and decreased the band gap energy from 3.57 to 3.10 eV. The highest PCE (power conversion efficiency) was obtained from the device fabricated with SnO_2 nanocrystallites calcined at a temperature of 300 °C, which was 0.0024%. This result was obtained due to the highest transmittance of this sample as compared to others; the higher the transmittance, the better the performance of the ETL, which in turn increased the overall efficiency of the PSC.

Keywords: *SnO_2 nancrystallites, co-precipitation method, calcination temperature, electron transport layer, perovskite solar cell*

1. INTRODUCTION

Richard Feynman's 1959 scientific speech entitled "There is Plenty Room at the Bottom" paved the way for the rapid development of nanotechnology in today's modern world, from the processes of synthesis and characterization to its applications [1]. An example of its development is the application of metal oxide in gas sensors [2], lithium-ion batteries [3], and solar cells [4]. One of the metal oxides with excellent potential for the development of nanotechnology in Indonesia is SnO_2 (tin oxide). Indonesia has scored in tin production through PT. Timah Tbk, with an increase of 128.7% in 2019 and a total production of 73,390 tons from the previous 33,444 tons in 2018 [5].

The use of nanomaterials, especially in the field of renewable energy, has continued to grow

DOI : 10.55981/metalurgi.687

Metalurgi is Sinta 2 Journal (https://sinta.ristekbrin.go.id/journals/detail?id=3708) accredited by Ministry of Research & Technology, Republic Indonesia

until now. It is such a significant opportunity to utilize solar energy sources in Indonesia. With an average daily intensity of solar radiation of 4.8 kWh/m2, Indonesia has the potential to generate more than 207 gigawatts of electrical energy from solar energy sources, beating out hydro, hydrothermal, wind, and ocean waves [6]. The advancement of solar cells, particularly PSC (perovskite solar cells), is needed as an alternative to renewable energy in Indonesia. Concerning this strategic point, SnO_2 could be utilized as an ETL (electron transport layer) material in PSCs.

SnO_2 was chosen as an alternative ETL material due to its excellent electron mobility properties (240 $cm^2/(V.s)$) [7]. In addition, SnO_2 can also be synthesized at low temperatures and produce high efficiency and good PSC stability [8]. Among the various chemical methods for metal oxide nanoparticle preparation, the co-precipitation method has shown good advantages, such as not requiring high temperatures and pressures. Also, filtration and washing can eliminate any impurities left over from the reaction process [9].

In this paper, SnO_2 nanocrystallites were synthesized using local $SnCl_4$ (tin chloride) from PT. Timah Industri by co-precipitation method and calcination at 300, 400, 500, and 600 °C. According to the literature review, no similar research has been conducted on synthesizing SnO2 nanocrystallites for PSC applications from indigenous Indonesian materials. The characterization of the synthesized samples was carried out using XRD (x-ray diffraction), SEM (scanning electron microscope), and UV-Vis spectrophotometer. The PSC device was fabricated and consisted of SnO_2 nanocrystallites as the ETL, with a planar heterojunction architecture of ITO/SnO_2/$CH_3NH_3PbI_3$/Spiro-OMeTAD/Au used for the performance test.

2. Materials And Methods

2.1 Materials

The materials used in this study were tin (IV) chloride ($SnCl_4$, PT. Timah Industri), ammonium hydroxide (NH_4OH, Merck), hydrochloric acid (HCl, fuming 37%, Merck), lead (II) iodide (PbI_2, Sigma Aldrich), methylammonium iodide (CH_3NH_3I, Greatcell Solar), dimethylformamide (DMF, Merck), polyethylene glycol (Triton X-100, Sigma Aldrich), Spiro-OMeTAD ($C_{81}H_{68}N_4O_8$, Solaronix), distilled water, acetone, ethanol, and ITO (indium tin oxide) glass substrate. All chemicals in this study were used without further purification.

2.2 Synthesis and Characterization of SnO_2 Nanocrystallites

In water solvent, 0.2 M $SnCl_4$ solution and 0.8 M NH_4OH solution were mixed and stirred until they formed a pH 9 homogenous solution. After that, the precipitate process was carried out for approximately 3 days until a white precipitate was formed, which was then filtered using Whatman filter paper No. 41 and washed with 100 ml of distilled water, and then the precipitate was separated again by the centrifugation method. The white precipitate was washed three times until the pH was close to 7 (neutral). The sample was then dried in an oven at 110 °C for 24 hours to obtain clear crystals of SnO_2, which were then mashed using a mortar to form a powder. Furthermore, the SnO_2 powder was calcined in a muffle furnace for 3 hours at 300, 400, 500, and 600 °C to be further analyzed using XRD (x-ray diffraction), SEM (scanning electron microscope), and UV-Vis spectrophotometer.

The estimation of the average crystallite size of SnO_2 nanocrystallites was calculated according to the following Scherrer's equation [10]:

$$D = \frac{k\lambda}{\beta cos\theta} \quad (1)$$

Where D is the average crystallite size (nm), k is the Scherrer constant (0.9), λ is the wavelength of X-rays, CuKα (1.5406 Å), β is the full width at half maximum/FWHM (radian), and θ is the diffraction angles (degrees).

The optical band gap energy (Eg) of synthesized materials was calculated from absorbance data by using Tauc's equation [11]:

$$(\alpha h\nu)^{1/n} = A(h\nu - E_g) \quad (2)$$

Where α is the absorbance coefficient, hν is the incident photon's energy, A is the proportional constant, and Eg is the optical band gap energy. The exponent value of n indicates the nature of the electron transition in the material, which can be ½ for the direct transition and 2 for the indirect transitions [12].

2.3 Fabrication of Perovskite Solar Cell

Preparation of the ITO glass substrate begins the first stage of PSC fabrication. The 1.5 × 2 cm ITO glass was covered with duct tape, and the rest section was etched with HCl for 15 minutes. Next, the duct tape was removed, and the ITO glass substrate was washed using an ultrasonic cleaner for 20 minutes with distilled water, acetone, and ethanol, respectively [13].

The second stage is the deposition of the SnO_2 layer onto the ITO glass, prepared in the first stage. SnO_2 slurry was made by mixing the SnO_2 powder with distilled water, acetone, ethanol, and PEG in a ratio of 3:2:4:2:2. This SnO_2 slurry solution was pulverized with a mortar so that it was evenly distributed. The slurry was then deposited onto the ITO glass by the doctor blade method and annealed in the open air at 110 °C for 1 hour [13].

The next stage is the coating of perovskite material ($CH_3NH_3PbI_3$ 0.8 M), obtained by mixing 276 mg PbI2 with 470 mg $CH_3NH_3PbI_3$. The mixed powder was dissolved in 5 mL of DMF and heated at 80 °C for 2 hours. A 100 µL perovskite solution was then dripped onto SnO_2-coated ITO glass and allowed to stand for one minute before spin coating at 3000 rpm for 30 seconds. The SnO_2@perovskite-coated ITO glass was heated at 150 °C for 1 hour in a muffle furnace [13].

Next is the HTL (hole transport layer) coating, which was obtained by dissolving 70 mg of Spiro-OMeTAD in 1 mL of chlorobenzene. After that, the solution was dripped onto SnO_2@perovskite-coated ITO glass and spin-coated for 30 seconds at 3000 rpm. Finally, a thin gold (Au) film was applied to the PSC (perovskite solar cells) configuration using the sputtering method at a pressure of 10-1 mbar and a current of 10 mA for 120 seconds [13]. The structure of the fabricated PSC layer is shown in Fig. 1.

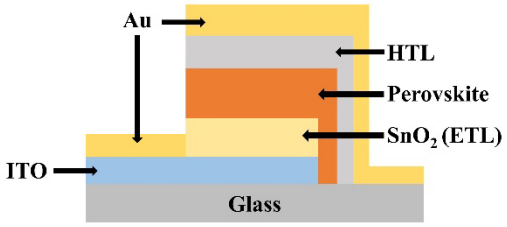

Figure 1. Perovskite solar cell layer structure with planar n-i-p heterojunction configuration

PSC performance testing was conducted to obtain the I-V curve using a semiconductor parameter analyzer (HP Agilent 4145B) with a standard illumination intensity of 100 mW/cm^2. The power conversion efficiency (PCE, η) was then calculated using the equation [14]:

$$\eta = \frac{FF \times I_{sc} \times V_{oc}}{I} \quad (3)$$

Where η is the PCE, is the fill factor, is the short-circuit photocurrent, is the open circuit voltage, and is the illumination intensity used during the test (100 mW/cm^2). While the value of FF was obtained by using the equation [14]:

$$FF = \frac{I_{max} \times V_{max}}{I_{sc} \times V_{oc}} \quad (4)$$

Where and are the current and voltage obtained from the maximum power on the I-V curve, which was obtained from the test results.

3. Result and Discussion

3.1 Crystal Structure Analysis

The formation of SnO_2 nanocrystallites begins with the formation of a white precipitate, $Sn(OH_4)$, in the gel phase, which results from the reaction of $SnCl_4$ with NH_4OH (Eq. (5)). When the white gel is dried, the water vapor is released, leaving behind white SnO_2 crystals (Eq. (6)) [15].

$$SnCl_4 + 4NH_4OH \rightarrow Sn(OH)_4 + 4NH_4Cl \quad (5)$$

$$Sn(OH)_4 \rightarrow SnO_2 + 2H_2O \quad (6)$$

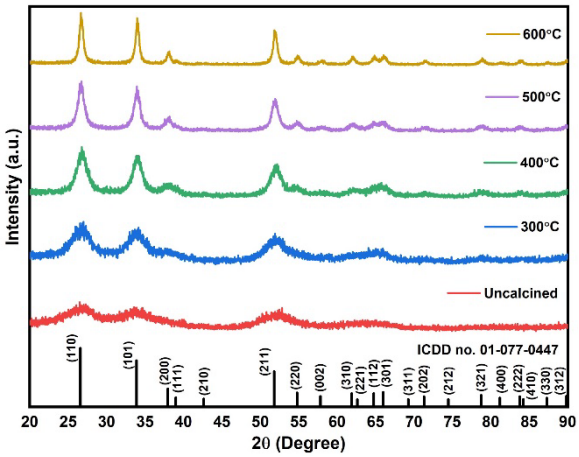

Figure 2. XRD pattern of SnO_2 nanocrystallites samples uncalcined and calcined at 300-600 °C

Figure 2 shows the x-ray diffraction pattern of SnO_2 nanocrystallite samples synthesized by the co-precipitation method with no calcination and with calcination at temperatures ranging from 300 to 600 °C. The diffraction peaks on the graph correspond to the crystal planes (110), (101), and (211) in the ICDD database No. 01-077-0447. This indicates that the synthesized samples had a rutile phase with a tetragonal structure. The graph depicts the sample's crystallinity increases with increasing calcination temperature. This shows that the calcination temperature substantially affect the formation of purified SnO_2 crystals.

According to the XRD graph, SnO_2 nanocrystallite samples that were calcined at temperatures higher than 300 °C have more excellent crystallinity than samples that were calcined at 300 °C or not calcined. When the calcination temperature is increased, the intensity of the diffraction peak becomes higher and sharper, and the width becomes narrower. This

indicates that the precursor obtains sufficient energy to form SnO_2 crystals [15].

The results of calculating the average crystallite size of SnO_2 nanocrystallites with the Scherrer equation (Eq. (1)) are presented in Table 1. The average crystallite size of samples that were not calcined and were calcined at temperatures ranging from 300 to 600 °C has increased from 1.19 to 13.75 nm.

Table 1. The estimation of average crystallite size of SnO_2 nanocrystallites obtained using the Scherrer equation

Calcination temperature (°C)	hkl	2θ (°)	FWHM	The average of crystallite size (nm)
	110	26.42	4.16	
	101	33.94	4.48	
Uncalcined	200	33.94	628.07	1.19
	211	57.68	9.38	
	220	57.90	7.59	
	110	26.76	3.24	
	101	33.84	3.15	
300	200	38.14	3.03	2.04
	211	52.12	3.93	
	220	55.73	617.68	
	110	26.79	1.68	
	101	34.03	1.49	
400	200	45.17	63.22	3.77
	211	52.04	1.82	
	220	65.36	2.76	
	110	26.69	1.17	
	101	33.97	1.04	
500	200	38.04	1.02	6.32
	211	51.92	1.06	
	220	54.56	130.15	
	110	26.72	0.69	
	101	34.01	0.64	
600	200	38.08	0.58	13.75
	211	51.95	0.66	
	220	54.89	0.55	

3.2 Optical Properties Analysis

Figure 3(a) depicts the optical absorbance spectrum of SnO_2 nanocrystallites samples. The curve shows a high absorbance in the ultraviolet region and a low absorbance in the visible light region. The absorbance peak of the sample shifted to the visible light region, or redshifted, as the calcination temperature increased from 300 to 500 °C. This phenomenon affects the optical band gap energy (E_g) of the SnO_2 nanocrystallites samples.

According to the calculation results of the Tauc method (Eq. (2)) in Table 2, the optical band gap energy tends to decrease with increasing calcination temperature, from 3.57 eV (uncalcined) to 2.81 eV (calcined at 500 °C). However, the optical band gap energy was discovered to rise 3.10 eV in the 600 °C calcined sample.

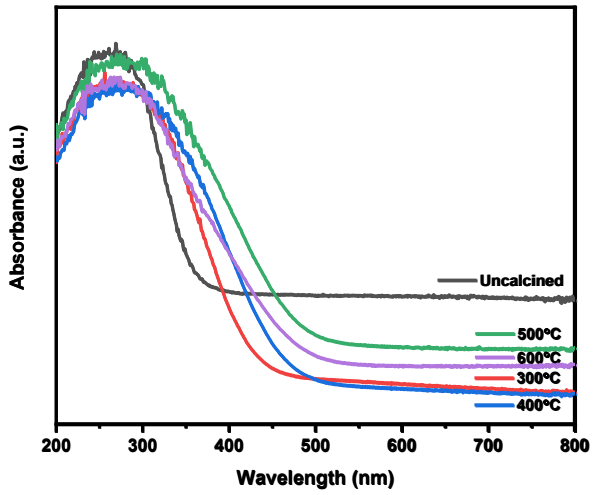

(a)

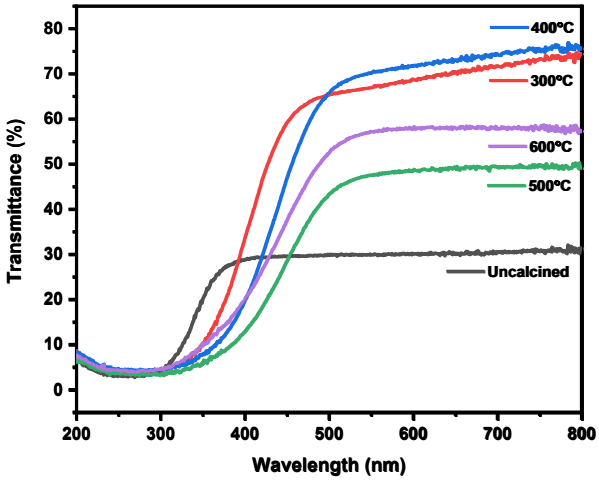

(b)

Figure 3. (a) Absorbance, and (b) transmittance spectra of SnO_2 nanocrystallites samples uncalcined and calcined at 300-600 °C

This conforms to the absorbance spectrum curve of the sample, which also underwent a blueshift.

Table 2. The optical band gap energy (E_g) with increasing calcination temperature

Calcination temperature (°C)	Band gap energy (eV)
Uncalcined	3.57
300	3.18
400	2.95
500	2.89
600	3.10

The size of the crystallite affects the optical band gap energy in a nanoparticle. Due to quantum effects, the band gap energy of the nanoparticle will decrease with increasing crystallite size and

vice versa [16]. In general, the decrease in band gap energy in the SnO_2 samples was consistent with the XRD analysis results, which demonstrated that the average crystallite size grows as the calcination temperature rises.

In the case of the 600 °C calcined sample, the band gap energy has increased again. Meanwhile, the crystallite size has increased due to the received heat energy driving force. There is a possibility that other phases may emerge in minor quantities, which are undetectable by XRD testing but perform an important role in influencing the mechanism of electron excitation from the valence band to the conduction band of SnO_2 nanocrystallites in this study. These nanocrystallites were discovered by UV-Vis spectroscopy at the absorption edge and represented by the optical band gap energy measurement results. However, additional characterization with more advanced tools, such as XANES and XPS, is required to confirm this.
Another explanation that can be related is the influence of the calcination temperature, which has a part in controlling the intrinsic defect in the SnO_2 crystal [17]. The higher the calcination temperature, the more significant the defect reduction, particularly oxygen vacancy, which increases the optical band gap energy [18]. This also happened in a study by Kamble et al., [19], which confirmed an increase in optical band gap energy due to defect reduction of SnO_2 nanocrystallites after the calcination process at 800 °C for 2 hours.

As ETL (electron transport layer) materials, SnO_2 nanocrystallite samples must have high transmittance. So that photons can easily pass through the ETL to the perovskite layer, where electron charge excitation occurs. The overall performance of the PSC (perovskite solar cells) improves with increasing transmittance of the ETL material [20]. For further analysis, the absorbance spectrum of the SnO_2 nanocrystallite samples was processed to obtain the percentage of transmittance using the Lambert-Beer equation as follows [21].

$$T(\%) = 10^{(2-A)} \quad (7)$$

Where T is the percentage of transmittance (%) and A is the absorbance.

As shown in Figure 3(b), the above calculation results were then plotted as a curve between the transmittance percentage and wavelength. According to the transmittance curve, it can be seen that the percentage of transmittance of all SnO_2 nanocrystallites samples increased in the visible light area. Higher transmittance intensities were discovered in SnO_2 nanocrystallite samples that were calcined at 300 and 400 °C. However, the curve for the 300 °C calcined sample has a greater range of light transmittance areas than the curve for the 400 °C calcined sample. This indicates that more photons of light are transmitted to the ETL layer and excite electrons in the perovskite layer in that sample. Therefore, the ETL transmittance performance of the 300 °C calcined sample is greater than that of other samples.

3.3 Surface Morphology Analysis

The surface morphology of the synthesized samples is observable in Fig. 4. According to the SEM observations, the samples tend to aggregate. due to the use of mortar in refining clear SnO_2 crystals into fine SnO_2 powder, which has a very high surface energy that leads to the formation of agglomerates. This result can also be correlated to forming strong hydrogen bonds in the precipitate during the synthesis process [22].

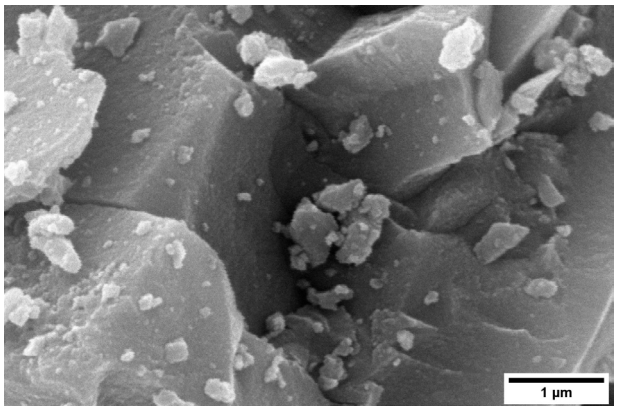

(a)

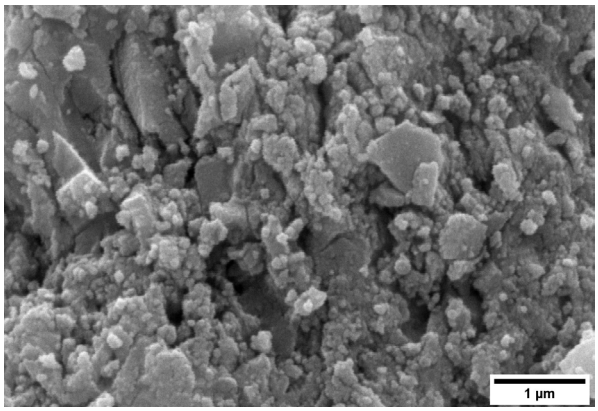

(b)

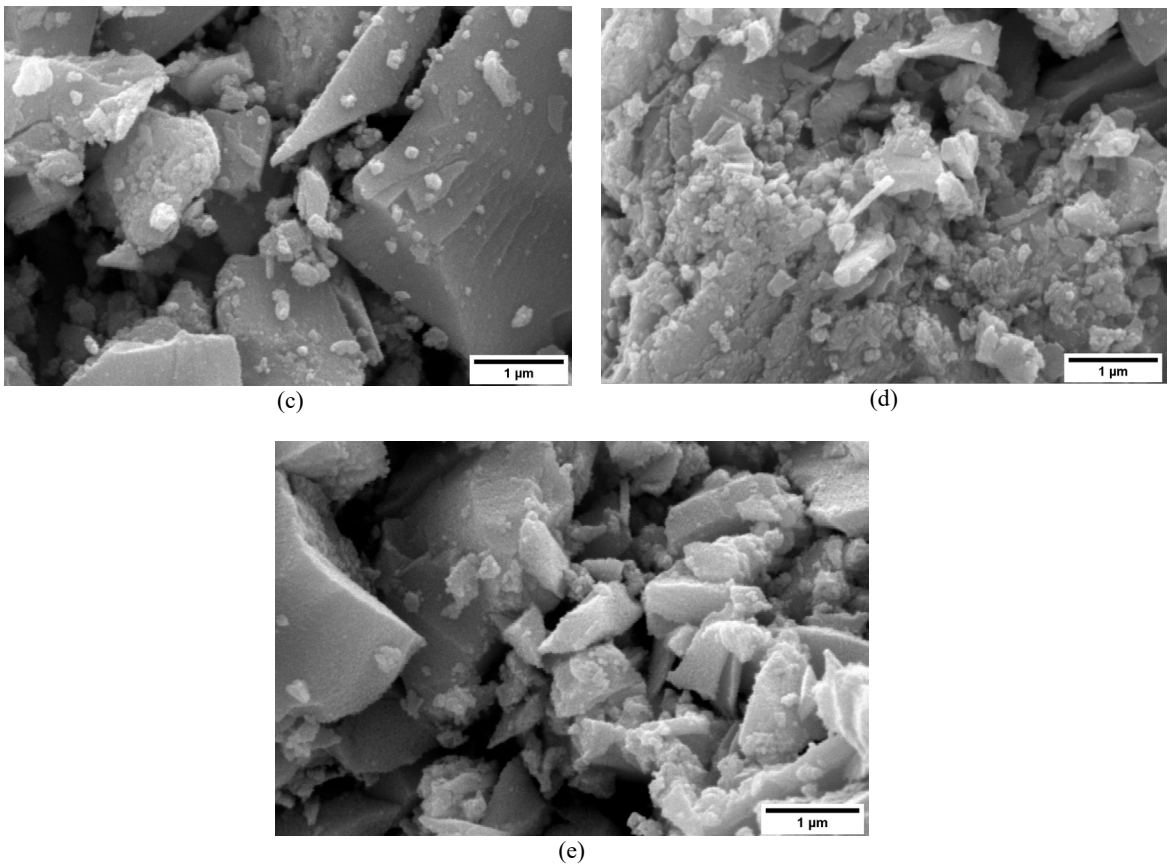

(c) (d)

(e)

Figure 4. Surface morphology of SnO_2 nanocrystallites samples (a) uncalcined and calcined at (b) 300, (c) 400, (d) 500, and (e) 600 °C

3.4 Perovskite Solar Cell Performance

The PSC configuration in this study consisted of ITO/SnO_2/$CH_3NH_3PbI_3$/Spiro-OMeTAD/Au. From the results of processing the I-V curve (Fig. 5), it was determined that only the SnO_2 nanocrystallites sample calcined at 300 °C could serve as an ETL layer and produced the highest PCE (power conversion efficiency), which was 0.0024% (Table 3). In this study, uncalcined and calcined SnO_2 nanocrystallite samples at temperatures other than 300 °C produced no difference in the I-V curve and thus did not affect the PCE.

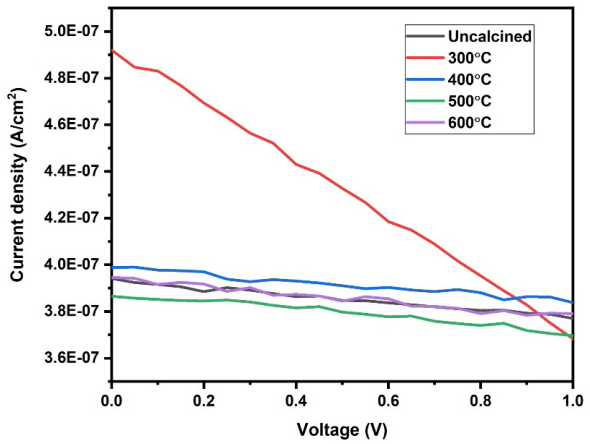

Figure 5. PSC I-V curve with ITO/SnO_2/$CH_3NH_3PbI_3$/Spiro-OMeTAD/Au configuraton

For comparison, in 2016, Jiang et al., [7] used a commercial tin precursor (Alfa Aesar) to produce SnO_2 nanoparticles as ETL through a low-temperature solution process. They achieved a high PCE of almost 20%. The work by Liu et al., [23] uses the same tin precursor and achieves high PCE of 19.38%.

The PSC device fabrication process using SnO_2 nanocrystallite samples, apart from the 300 °C calcined sample, had problems with uneven depositions of the SnO_2 layer onto the ITO glass using the doctor blade method. In addition, the perovskite layer fabrication process carried out in the open air and not in an inert environment also contributed to the low PCE obtained. It has been reported in other studies that most high-efficiency PSC devices are obtained by manufacturing a perovskite layer under inert conditions using a glove box [24].

It is recommended to preserve the substrate at an increased temperature for future fabrication of perovskite solar cell layers using doctor blade deposition in order to obtain a pinhole-free, uniform, and smooth coating. This will increase the solvent evaporation rate, promoting nucleation, and crystal growth [25].

4. CONCLUSION

SnO_2 nanocrystallites have been successfully synthesized using a local tin chloride precursor through the co-precipitation method and calcination treatment at various temperatures of 300, 400, 500, and 600 °C. The crystal structure characterization revealed that the higher the calcination temperature, the higher the crystallinity and the larger the average size of the formed SnO_2 nanocrystallites. The increasing size of crystallites also causes a reduction in band gap energy due to quantum effects. Thus, the calcination treatment in the co-precipitation method affects the characteristics of the resulting SnO_2 nanocrystallites. The SnO_2 nanocrystallites have been applied as an ETL material in PSC with a planar n-i-p heterojunction configuration composed of ITO/SnO_2/$CH_3NH_3PbI_3$/Spiro-OMeTAD/Au.

The highest PSC efficiency was achieved by PSC composed of SnO_2 nanocrystalline with a calcination temperature of 300 °C, which was 0.0024%. This result is following the transmittance level of the sample, which has a wider range of transmittance areas compared to other samples so that more photon energy can pass through the ETL and ultimately improve the overall PSC performance. In this study, the PSC efficiency is still very low. This is because of limitations during making the device, such as the thickness of the layers of the different structures that make up the solar cells and the non-inert condition in which the device is made.

Table 3. Photovoltaic characteristics of the perovskite solar cells based on different calcination temperature

Calcination temperature (°C)	V_{oc} (V)	I_{sc} (A/cm^2)	V_{maks} (V)	I_{maks} (A/cm^2)	FF	PCE (%)
Uncalcined	5	0.0001	2.7	0.0001	0.2922	0.0001
300	5	0.0013	3.35	0.0007	0.3747	0.0024
400	5	0.0001	2.9	0.0001	0.3975	0.0001
500	5	0.0001	2.7	0.0001	0.3038	0.0001
600	5	0.0001	2.5	0.0001	0.2834	0.0001

ACKNOWLEDGMENT

We gratefully acknowledge Direktorat Riset dan Pengabdian Masyarakat Universitas Indonesia (DRPM-UI) for research funding support through International Indexed Publication Grants (PUTI) 2020 (No. NKB-3702/UN2.RST/HKP.05.00/2020) and PT. Timah Industri for providing tin chloride precursor.

REFERENCES

[1] J. E. Hulla, S. C. Sahu, and A. W. Hayes, "Nanotechnology: History and future," *Hum. Exp. Toxicol.*, vol. 34, no. 12, pp. 1318-1321, 2015. Doi: 10.1177/0960327115603588.

[2] W. Chen, Q. Zhou, F. Wan, and T. Gao, "Gas sensing properties and mechanism of nano-SnO_2-based sensor for hydrogen and carbon monoxide," *J. Nanomater.*, vol. 2012, no. 612420, 2012. Doi: 10.1155/2012/612420.

[3] C. P. Wu, K. X. Xie, J. P. He, Q. P. Wang, J. M. Ma, S. Yang, and Q. H. Wang, "SnO_2 quantum dots modified N-doped carbon as high-performance anode for lithium ion batteries by enhanced pseudocapacitance," *Rare Met.*, vol. 40, no. 1, pp. 48-56, 2021. Doi: 10.1007/s12598-020-01623-x.

[4] H. Min, D. Y. Lee, J. Kim, G. Kim, K. S. Lee, J. Kim, M. J. Paik, Y. K. Kim, K. S. Kim, M. G. Kim, T. J. Shin, and S. I. Seok, "Perovskite solar cells with atomically coherent interlayers on SnO_2 electrodes," *Nature*, vol. 598, no. 7881, pp. 444-450, 2021. Doi:10.1038/s41586-021-03964-8.

[5] PT. Timah Tbk.," Membangun ketahanan dan meraih performa progresif," Laporan Tahunan Annual Report 2021. Available: https://timah.com/userfiles/post/220428626A5287E3839.pdf. [Diakses tanggal: 26 Juli 2022]

[6] Pusat Pengkajian Industri Proses dan Energi (PPIPE)," Outlook energi Indonesia 2021 perspektif teknologi energi Indonesia: Tenaga surya untuk penyediaan energi charging station," Badan Pengkajian dan Penerapan Teknologi (BPPT). Jakarta. Available: https://www.bppt.go.id/dokumen/file/865/download [Diakses tanggal: 26 Juli 2022]

[7] Q. Jiang, L. Zhang, H. Wang, X. Yang, J. Meng, H. Liu, Z. Yin, J. Wu, X. Zhang, and J. You, "Enhanced electron extraction

using SnO_2 for high-efficiency planar-structure $HC(NH_2)_2$ PbI_3-based perovskite solar cells," *Nat. Energy*, vol. 2, no. 1, 2017. Doi:10.1038/nenergy.2016.177.

[8] G. Yang, P. Qin, G. Fang, and G. Li, "Tin oxide (SnO_2) as effective electron selective layer material in hybrid organic-inorganic metal halide perovskite solar cells," *J. Energy Chem.*, vol. 27, no. 4, pp. 962-970, 2018. Doi: 10.1016/j.jechem.2018.03.018.

[9] S. Tazikeh, A. Akbari, A. Talebi, and E. Talebi, "Synthesis and characterization of tin oxide nanoparticles via the co-precipitation method," *Mater. Sci. Pol.*, vol. 32, no. 1, pp. 98-101, 2014. Doi: 10.2478/s13536-013-0164-y.

[10] C. Karunakaran, S. Sakthi Raadha, and P. Gomathisankar, "Microstructures and optical, electrical and photocatalytic properties of sonochemically and hydrothermally synthesized SnO_2 nanoparticles," *J. Alloys Compd.*, vol. 549, pp. 269-275, 2013. Doi: 10.1016/j.jallcom.2012.09.035.

[11] Ł. Haryński, A. Olejnik, K. Grochowska, and K. Siuzdak, "A facile method for Tauc exponent and corresponding electronic transitions determination in semiconductors directly from UV–Vis spectroscopy data," *Opt. Mater. (Amst).*, vol. 127, 2022. Doi: 10.1016/j.optmat.2022.112205.

[12] Y. Wang, L. Tan, and L. Wang, "Hydrothermal synthesis of SnO_2 nanostructures with different morphologies and their optical properties," *J. Nanomater.*, vol. 2011, no. 529874, 2011. Doi: 10.1155/2011/529874.

[13] N. Sofyan, A. Ridhova, Salman, A. H. Yuwono, and A. Udhiarto, "Synthesis and characterization of nano rosette TiO_2 and $CH_3NH_3PbCl_2I$ for potential use in perovskite solar cell," *IOP Conf. Ser. Mater. Sci. Eng.*, vol. 541, no. 1, 2019. Doi:10.1088/1757-899X/541/1/012048.

[14] S. Günes, and N. S. Sariciftci, "Hybrid solar cells," *Inorganica Chim. Acta*, vol. 361, no. 3, pp. 581-588, 2008. Doi: 10.1016/j.ica.2007.06.042.

[15] P. Khaenamkaew, D. Manop, C. Tanghengjaroen, and W. P. N. Ayuthaya, "Crystal structure, lattice strain, morphology, and electrical properties of SnO_2 nanoparticles induced by low calcination temperature," *Adv. Mater. Sci. Eng.*, vol. 2020, no. 3852421, 2020. Doi: 10.1155/2020/3852421.

[16] R. Viter, A. Katoch, and S. S. Kim, "Grain size dependent bandgap shift of SnO_2 nanofibers," *Met. Mater. Int.*, vol. 20, no. 1, pp. 163-167, 2014. Doi: 10.1007/s12540-013-6027-6.

[17] S. Mehraj, M. S. Ansari, and A. A. Al-ghamdi, "Annealing dependent oxygen vacancies in SnO_2 nanoparticles: structural, electrical and their ferromagnetic behavior," *Mater. Chem. Phys.*, vol. 171, pp. 109-118, 2016. Doi: 10.1016/j.matchemphys.2015.12.006.

[18] J. Ungula, B. F. Dejene, and H. C. Swart, "Effect of pH on the structural, optical and morphological properties of Ga-doped ZnO nanoparticles by reflux precipitation method," *Phys. B Condens. Matter*, vol. 535, pp. 251-257, 2018. Doi:10.1016/j.physb.2017.07.052.

[19] V. B. Kamble, and A. M. Umarji, "Defect induced optical bandgap narrowing in undoped SnO_2 nanocrystals," *AIP Adv.*, vol. 3, no. 8, 2013. Doi: 10.1063/1.4819451.

[20] Y. Chen, Q. Meng, L. Zhang, C. Han, H. Gao, Y. Zhang, and H. Yan, "SnO_2-based electron transporting layer materials for perovskite solar cells: A review of recent progress," *J. Energy Chem.*, vol. 35, pp. 144-167, 2019. Doi: 10.1016/j.jechem.2018.11.011.

[21] D. F. Swinehart, "The beer-lambert law," *J. Chem. Educ.*, vol. 39, no. 7, pp. 333, 1962.

[22] J. Divya, A. Pramothkumar, S. J. Gnanamuthu, D. C. B. Victoria, and P. C. J. Prabakar, "Structural, optical, electrical and magnetic properties of Cu and Ni doped SnO_2 nanoparticles prepared via co-precipitation approach," *Phys. B Condens. Matter*, vol. 588, no. 2019, pp. 412169, 2020. Doi: 10.1016/j.physb.2020.412169.

[23] J. Liu, N. Li, Q. Dong, J. Li, C. Qin, and L. Wang, "Tailoring electrical property of the low-temperature processed SnO_2 for high-performance perovskite solar cells," *Sci. China Mater.*, vol. 62, no. 2, pp. 173-180, 2019. Doi:10.1007/s40843-018-9305-6.

[24] M. Lv, X. Dong, X. Fang, B. Lin, S. Zhang, X. Xu, J. Ding, and N. Yuan, "Improved photovoltaic performance in perovskite solar cells based on $CH_3NH_3PbI_3$ films fabricated under

controlled relative humidity," *RSC Adv.*, vol. 5, no. 114, pp. 93957-93963, 2015. Doi:10.1039/c5ra14587b.

[25] D. Wang, J. Zheng, X. Wang, J. Gao, W. Kong, C. Cheng, and B. Xu, "Improvement on the performance of perovskite solar cells by doctor-blade coating under ambient condition with hole-transporting material optimization," *J. Energy Chem.*, vol. 38, pp. 207-213, 2019. Doi:10.1016/j.jechem.2019.03.023.

METALURGI
Majalah Ilmu dan Teknologi
p-ISSN 0126-3188 | e-ISSN 2443-3926
ejurnalmaterialmetalurgi.lipi.go.id

RECOVERY OF MANGANESE FROM MANGANESE ORE REDUCTIVE ACID LEACHING PROCESS USING REEDS (IMPERATA CYLINDRICA) AS REDUCING AGENT

Lalu Suhaimi*, Samsul Bahtiar, Andi Sarina, Khairunnisya
Metallurgical Engineering, Sumbawa University of Technology
Jl. Raya Olat Maras, Kabupaten Sumbawa, Nusa Tenggara Barat, Indonesia 84371
*E-mail: lalu.suhaimi@uts.ac.id

Received: 09-03-2023, Revised: 17-04-2023, Accepted: 08-05-2023

Abstract

Recovery of manganese from manganese ores was investigated by reductive leaching method using reeds as a reductant in the sulfuric acid medium. Cellulose, hemicellulose, and lignin are natural reducing agents which are widely used as reducing agents to recover manganese. Effects of calcination temperature and the holding time calcination on the leaching efficiency of manganese and impurities were examined. The calcination temperature and the holding time calcination have a significant effect on the extraction of manganese. The experimental results demonstrated that the higher the calcination temperature used, the higher the percentage of manganese obtained, namely 79.58% and 87.38%, respectively. The XRD (x-ray diffraction) pattern shows that the manganese phases formed at 700 and 800 °C are Mn_3O_4 (hausmannite) and Mn_2O_3 (bixbite), respectively. The morphology in the sample with calcination temperature at 700 °C showed agglomerate- shaped particles and unevenly dispersed. Meanwhile, the sample with calcination temperature at 800 °C exhibited agglomerated particles of inhomogeneous size and were more evenly distributed. Variation of holding time in the manganese ores recovery process also affects the results of manganese recovery. The composition of the manganese recovery in the samples using holding time calcination variations of 3 and 4 hours was 83.88% and 89.24%, respectively. The results of the XRD analysis showed that the manganese phase formed using 3 hours of calcination holding time was dominated by Mn_3O_4 (hausmannite). Meanwhile, the manganese phase formed using 4 hours of holding time of calcination was dominated by Mn_2O_3 (bixbite).

Keywords: *Reeds, manganese, reductant, Mn_3O_4 (haussmannite), Mn_2O_3 (bixbite)*

1. INTRODUCTION

Global warming, as a result of increased GHGs (greenhouse gas) emission activities, has a severe impact on people's survival. One reason for the increasing of GHGs emissions is the production of ever-increasing amounts of carbon. Transportation is one of the contributing sectors to increasing carbon production. Therefore, a strategy is needed to reduce GHGs emissions in transportation.

One strategy that can be implemented to reduce GHG emissions caused by transportation is by switching to the use of electric transportation. Electric vehicles have advantages over ICE (internal combustion engine) based vehicles in reducing air pollution and GHG emissions. Electric vehicles produce far less air pollution and can be near zero compared to ICE (internal combustion engine) based vehicles [1].

Using electric transportation as a strategy to reduce GHGs emissions has encouraged researchers, especially in the fields of materials science and engineering, to continue to innovate to meet battery needs and obtain the increasing battery performance that continously. The battery in an electric car or motorcycle functions as an energy storage device in the form of DC (direct current) electricity.

Manganese is one of the materials developed by researchers to be applied as a component of battery systems [2]-[5]. In nature, manganese ore can be found in various forms. For example, MnO_2 (pyrolusite), $BaMn_9O_{16}(OH)_4$ (psilomelane), Mn_2O_3 (manganese), Mn_3O_4

DOI : 10.55981/metalurgi.705

Metalurgi is Sinta 2 Journal (https://sinta.ristekbrin.go.id/journals/detail?id=3708) accredited by Ministry of Research & Technology, Republic Indonesia

(haussmannite), Mn_2O_3 (manganite), Mn_3O_4 (haussmannite), $MnCO_3$ (rodhochrosite), and $MnSiO_3$ (rhodonite). The investigation on the processing of manganese ores with a content of less than 40% through hydrometallurgical processes has been carried out in recent years [6]. The type of reducing agent is the important factor influencing the recovery process of manganese ore using the hydrometallurgical method. Generally, the types of reducing agents used are inorganic and organic. Inorganic reductant substances such as SO_2 (sulfur dioxide), Fe_2SO_4 (ferrous sulfate), iron powder, and other iron salts have disadvantages compared to the organic reducing agents [6]. One of the deficiencies of using inorganic reductants as reducing agents is that they are not eco-friendly. Therefore, one of the solutions is using reductants derived from agriculture or biomass.

Cellulose, hemicellulose, and lignin are natural reducing agents which are widely used as reducing agents to recover manganese. This type of reducing agent is commonly found in agriculture or biomass. Wu et.al. [7] has carried out manganese recovery from low-grade manganese ores using cellulose as the reducing agent. The results showed that the amount of manganese obtained was more than 90%. Xiong et al., [8] have studied the leaching process of low-grade pyrolusite using a lignin-reducing agent with 2M H_2SO_4 solvent. This study obtained manganese with a percentage of more than 91%. Ali et al., [9] have succeeded in the recovery of manganese with a percentage of 92,48% from a high-grade manganese ore under similar conditions by using 4% corncob as a reducing agent at 90 °C.

One of the plants that are easily found in nature that contains cellulose, hemicellulose, and lignin is reeds. Reeds (*imperata cylindrica*) contain about 40.22% cellulose, so this plant can potentially be optimized as reducing agents to recover manganese from their ores [10]. Furthermore, reeds (*imperata cylindrica*) are abundant plants in Indonesia and have yet to be utilized optimally. Based on this, this research will recover manganese ore obtained from West Sumbawa Regency, West Nusa Tenggara Indonesia, by using reeds (*imperata cylindrica*) as a reducing agent.

2. MATERIALS AND METHODS

The process of recovering manganese from its ores in this research was carried out in several stages. The first, is making reducing agent from reeds (*Imperata Cylindrica*). Second, the process of manganese recovery using the leaching method.

2.1 The Process of Making Natural Reducing Agents from Reeds (*Imperata Cylindrica*)

The fabrication of the reductor agent was strated with the reed washing process. The reeds were soaked in water for two hours. After that, the reeds were dried under the rays of the sun. The dried reeds were then cut into small pieces, mashed using a blender, and sieved. 5 grams of reed powder was macerated using 17.5% NaOH solution for 48 hours. After that, the sample was filtered using filter paper. The precipitate obtained from the maceration process is then washed using water. The sample was then dried using an oven until a dry precipitate was obtained.

2.2 The Recovery Process of Manganese Ores

The leaching process of manganese ores begins with the process of refining the manganese ores. The refined manganese ores were then dried using an oven at a temperature of 110 ℃ for 1 hour to remove the moisture content. The next step is the process of hydrolysis. The hydrolysis process was done by mixing 20 grams of manganese ores and 5 grams of reed powder using 100 ml of 5% H_2SO_4 acid solution. The mixture was then stirred using a magnetic stirrer with 700 rpm of speed for 2 hours at a temperature of 90 ℃. The mixture obtained from this process was filtered to separate the filtrate and residue.

The filtrate obtained from hydrolysis was then precipitated by adding NaOH solution to the filtrate until a pH of 9 was obtained. The following process was to separate the deposit and the filtrate using filter paper. The precipitate obtained was then washed until it reached a neutral pH. The samples from the deposition process were then dried by using an oven at a temperature of 100 ℃ for one hour. The dried samples then calcined with temperature variations and in holding time calcination.

2.3 Sample Characterization

Samples that had been calcined at various temperatures of 700 and 800 ℃ and holding times of 3 and 4 hours were characterized. The characterization carried out on the samples included XRF (x-ray fluorescence), Brand: PANalytical, Type: Minipal 4. The characterization of the sample by using XRF aims to determine the percentage of manganese (purity) obtained. Characterization to determine the phase formed in the sample was carried out using XRD (x-ray diffraction), Brand:

PANalytical, Type: Expert Pro and characterization using SEM (scanning electron microscopy), Brand: FEI, Type: Inspect-S50 used to see the microstructure manganese powder.

3. Result and Discussion

3.1 Various Calcination Temperatures

Table 1 shows the composition of the chemical elements contained in the precipitate from leaching after the recovery process was carried out using a calcination temperature of 700 ℃ which was analyzed using XRF (x-ray fluorescence). According to Table 1, the percentage of recovering manganese from its ores is 79.58%.

Table 1. The results of XRF analysis the sample with temperature calcination of 700 ℃

Elemen	Wt.%
Al	5.50
P	0.51
S	6.40
Ca	1.69
Mn	79.58
Cu	0.12
Zn	0.63
As	0.53
Mo	4.80
Re	0.30

Meanwhile, Table 2 shows the XRF analysis results of samples with a calcination temperature of 800 °C. The percentage of manganese recovery from manganese ores with a calcination temperature of 800 °C is 87.38%.

Table 2. The results of XRF analysis with temperature calcination of 800 ℃

Element	Wt.%
Al	1.50
P	0.10
S	3.90
Ca	0.51
Mn	87.38
Cu	0.13
Zn	0.57
As	0.88
Mo	4.80
Re	0.20

Based on the results of the XRF analysis of these samples, it was shown that a higher calcination temperature would result in a greater percentage of manganese recovery.

Figure 1 shows the results of the phase analysis of manganese samples recovered from manganese ores. Based on the XRD (x-ray diffraction) analysis, most of the manganese phase formed at a calcination temperature of 700 ℃ is dominated by bixbite (Mn_2O_3). Meanwhile, the impurities are not detected by the XRD instrument because the composition of these impurities is small. The Mn_3O_4 phase peak was detected at 2θ, ~18.022°; ~28.927°; ~32.395°; ~36.103°; ~38.105°; ~44.435°; ~50.857°; ~56.053°; ~58.533°; and ~59.938°, respectively corresponding to the crystal plane (101); (112); (103); (211); (004); (220); (105); (303); (321); and (224).

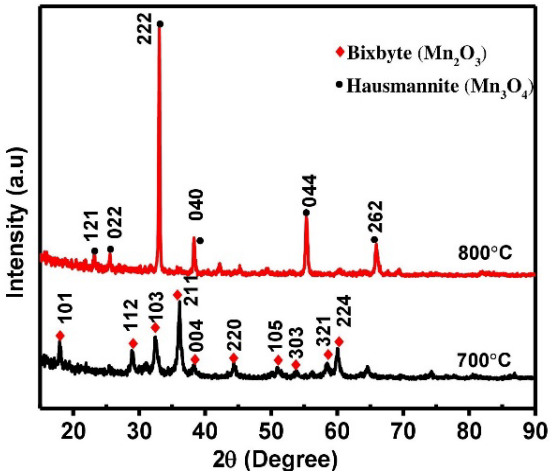

Figure 1. X-ray diffraction patterns for Mn recovered from manganese ores with calcination temperatures of 700 ℃ and 800 ℃

Meanwhile, the sample with a calcination temperature of 800 ℃ was dominated by manganese phase in the form of hausmannite (Mn_3O_4) which was detected at 2θ peaks: ~23.139°; ~26.781°; ~32.854°; ~38.235°; ~55.183°; and ~65.791° respectively correspond to the crystal planes (121), (022), (222), (040), (044), and (262). These data are also supported by the research conducted by Lan et al., [11] where calcination temperature plays an important role in the structure and the morphology of modifications. The difference in the formation of compounds resulting from calcination is because high temperatures can move the atoms to change the mineral structure into a new structure, and atomic diffusion also occurs accompanied by the release of organic compounds. Furthermore, temperature differences during the calcination process cause changes in the manganese oxide compound from the pyrochroite type to manganese oxide in various forms. The mechanism for changing the structure of pyrochroite to MnO_2 and Mn_2O_3 occurs because the pyrochroite atoms vibrate, and the arms between atoms are elongated due to heat energy in the calcination process. The process of changing the structure is caused by an increase in

heat and dissolution or dissolution of atoms contained in the oxidation area, which is the ion exchange area [12].

Figure 2 shows the microstructure of the samples at the variation calcination temperatures of 700 and 800 ℃ (Figs. 2(a) and 2(b)) which were characterized using SEM (scanning electron microscope).

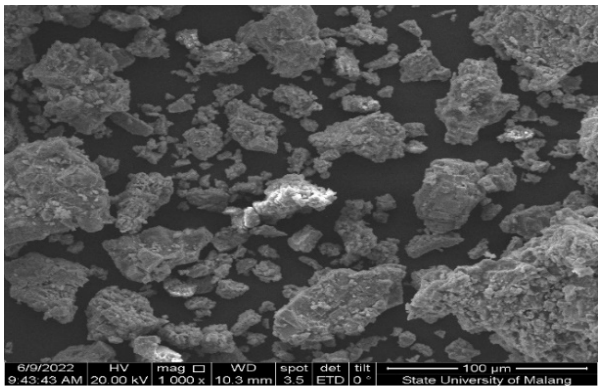

(a)

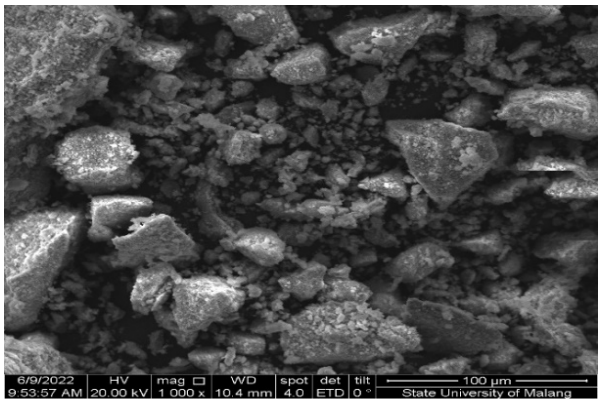

(b)

Figure 2. The SEM images of the sample calcined at (a) 700 ℃, and (b) 800 ℃

According to SEM analysis, the morphology of the hausmannite manganese oxide phase is in the form of agglomerated powder particles, and the powder particles are not evenly distributed (Fig. 2(a)). Meanwhile, the sample calcined at 800 ℃ (Fig. 2(b)) showed the morphology of the bixbite oxide phase (Mn_2O_3) in the form of agglomerated particles with inhomogeneous sizes and evenly distributed.

3.2 Various Holding Time Calcination

Table 3 shows the percentage of elemental content found in manganese ore after the recovery process was carried out using reeds as the reducing agent with a calcination time of 3 hours with a calcination temperature of 700 ℃. According to Table 3, the percentage of recovering manganese from its ores is 83.88%.

Figure 3 shows the results of the analysis of the phases formed in each sample. According to the results of the XRD analysis, most of the manganese phase formed using 3 hours of holding time calcination was dominated by the hausmannite (Mn_3O_4) phase.

Table 3. The results of an XRF analysis of a sample with a holding time of 3 hours and a calcination temperature of 700 °C

Element	Composition (%)
Al	3.80
P	0.20
S	3.60
Ca	1.64
Mn	83.88
Cu	0.10
Zn	0.60
As	0.72
Mo	4.50
Re	0.20
Bi	0.33

Meanwhile, Table 4 shows the recovering manganese from its ores with a holding time of calcination at 4 hours with a calcination temperature of 700 ℃. The composition percentage of recovering manganese with the holding time calcination of 4 hours is more significant than the holding time calcination of 3 hours, which is 89.24%. Characterizing the sample using XRF, shows that the longer the holding time calcination, the higher the recovery of the manganese obtained.

Table 4. The results of an XRF analysis of a sample with a holding time of 4 hours and a calcination temperature of 700 °C

Element	Composition (%)
Al	1.30
P	0.10
Si	0.60
S	2.30
Ca	0.52
Mn	89.24
Cu	0.10
Zn	0.63
As	0.70
Mo	4.00
Re	0.20

Meanwhile, the dopants are not detected by the XRD instrument because the composition of these dopants is small. The peak of the hausmannite phase was detected at 2θ, ~18.014°; ~30.990°; ~32.383°; ~36.084°; ~58,500°; and ~59,910° respectively corresponding to the

crystal plane (101); (112); (103); (200); (103); (211); (321); and (224). The peak of the most dominant Mn_2O_3 phase is detected at the peak of 2θ: ~32.954°, corresponding to the crystal's plane (222).

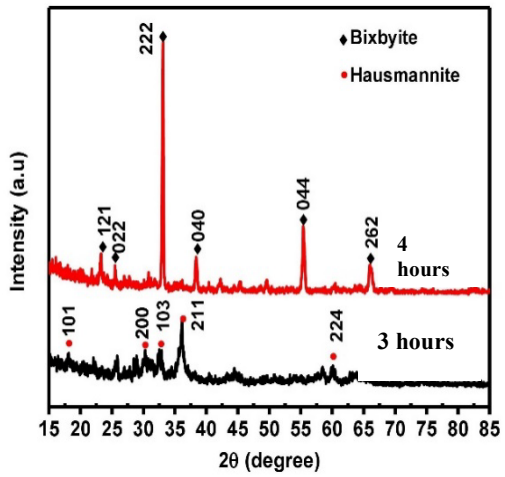

Figure 3. X-ray diffraction patterns for Mn recovered from manganese ores with holding time calcination of 3 and 4 hours

Other Mn_2O_3 phase peaks formed at 2θ, ~23.139°; ~26.781°; ~38.235°; ~55.183° and ~65.791° correspond to the crystal planes (121), (022), (040), (044), and (262), respectively.

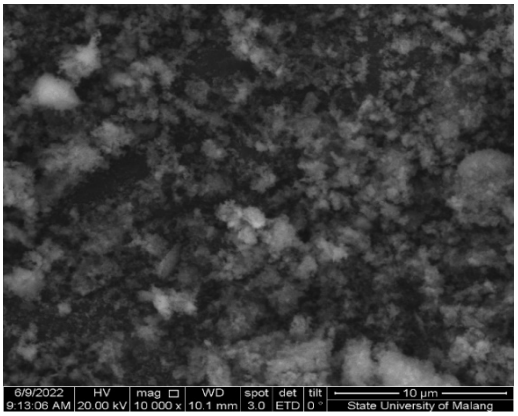

(a)

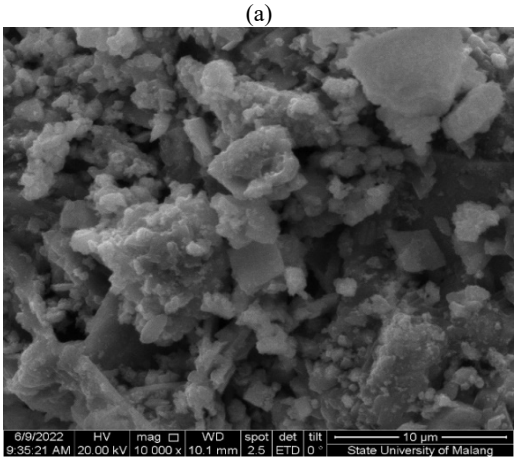

(b)

Figure 4. SEM images of the sample with holding time calcination at (a) 3 hours, and (b) 4 hours

Meanwhile, in samples with a calcination holding time of 4 hours, the manganese phase formed was dominated by the bixbite (Mn_2O_3) phase.

Figure 4 shows the microstructure of the samples using 3 and 4 hours of calcination holding times (Figs. 4(a) and 4(b)), which were characterized by using SEM with 1000x magnification. The sample using 3 hours of holding times calcination showed the morphologically formed plate particles (Figure 4(a)). Meanwhile, the sample using 4 hours of holding times calcination showed the morphology of the bixbite oxide phase (Mn_2O_3) in the form of flake particles that were evenly distributed (Fig. 4(b)).

4. CONCLUSION

The recovery of manganese ores obtained from West Sumbawa Regency, West Nusa Tenggara, Indonesia, using reeds (Imperata Cylindrica) as the reducing agent, has been successfully investigated. Increasing the temperature of the calcination process generates an increased percentage of manganese from 79.58% to 87.38%. Increasing the calcination temperature also changes the structure of the sample. In addition, putting temperature variation in the calcination process produces different morphological patterns.

Increasing the holding time of the calcination process generates an increased percentage of manganese from 83.88% to 89.24%. Besides, increasing the holding time also changes the structure obtained from the sample. Furthermore, different holding times in the calcination process produce different morphological patterns.

ACKNOWLEDGMENT

The authors thank the Sumbawa University of Technology for the laboratory facilities.

REFERENCES

[1] C. Sudjoko, "Strategi pemanfaatan kendaraan listrik berkelanjutan sebagai solusi untuk mengurangi emisi karbon," *Jurnal Paradigma: Jurnal Multidisipliner Mahasiswa Pascasarjana Indonesia*, vol. 2, no. 2, pp. 54-68, 2021. Doi: 10.22146/jpmmpi.v2i2.70354

[2] V. Mathew, B. Sambandam, S. Kim, K. Sungjin, S. Park, S. Lee, M. H. Alfaruqi, V. Soundhararajan, S. Islam, D. Y. Putro, J. Y. Hwang, Y. K. Sun, and K. Jaekook, "Manganese and vanadium oxide cathodes for aqueous rechargeable zinc-ion batteries: a

focused view on performance, mechanism, and developments," *ACS Energy Lett.*, vol. 5, no. 7, pp. 2376-2400, 2020. Doi: 10.1021/acsenergylett.0c00740.

[3] M. H. Alfaruqi., S. Islam, D. Y. Putro, V. Mathew, S. Kim, J. Jo, K. Seokhun, Y. K. Sun, K. Kwangho, and K. Jaekook, "Structural transformation and electrochemical study of layered MnO_2 in rechargeable aqueous zinc-ion battery," *Electrochim. Acta*, vol. 276, pp. 1-11, 2018. Doi:10.1016/j.electacta.2018.04.139.

[4] S. Islam, M.H. Alfaruqi, J. Song, S. Kim, D.T.Pham, J. Jo, K. Seokhun, V. Mathew, J.P. Baboo, Z. Xiu and K. Jaekook, " Carbon-coated manganese dioxide nanoparticles and their enhanced electrochemical properties for zinc-ion battery applications, " *Journal of energy chemistry, vol.* 276, pp. 815-819, 2017.

[5] R. Farzana, K. Hassan, and V. Shajwalla, " Manganese oxide synthesized from spent Zn-C battery for supercapacitor electrode application," scientific reports*, vol.* 9, pp. 1-12, 2019.

[6] M. J. Pereira, M. M. F. Lima, and R. M. F. Lima, "Calcination and characterisation studies of a Brazilian manganese ore tailing," *Int. J. Miner. Process.*, vol. 131, pp. 26-30, 2014. Doi:10.1016/j.minpro.2014.08.003.

[7] F. F. Wu, H. Zhong, S. Wang, and S. F. Lai, "Kinetics of reductive leaching of manganese oxide ore using cellulose as reductant," *J. Cent. South Univ.*, vol. 21, no. 5, pp. 1763-1770, 2014. Doi:10.1007/s11771-014-2122-1.

[8] S. Xiong , X. Lia, P. Liua, S. Haoa, F. Haoa, Z. Yinb, and J. Liu "Recovery of manganese from low-grade pyrolusite ore by reductively acid leaching process using lignin as a low cost reductant," *Miner. Eng.*, vol. 125, pp. 126-132, 2018. Doi: 10.1016/j.mineng.2018.06.003.

[9] S. Ali, Y. Iqbal, K. Ahmad, and B. Afridi, "Phase, microstructure and beneficiation of manganese ore by acid leaching," *Journal of Minerals and Materials Characterization and Engineering*, vol. 6, no.1. pp. 60-71, 2018. Doi:10.4236/jmmce.2018.61006.

[10] S. D. Kartikasari, S. Nurhatika, and A. Muhibuddin, "Potensi alang-alang (Imperata cylindrica) dalam produksi etanol menggunakan bakteri zymomonas mobilis," *Jurnal Sains dan Seni ITS*, vol. 2, no. 2, 2013. Doi:10.12962/j23373520.v2i2.3741.

[11] L. Lan, Q. Li, G. Gu, H. Zhang, and B. Liu, "Hydrothermal synthesis of γ-MnOOH nanorods and their conversion to MnO_2, Mn_2O_3, and Mn_3O_4 nanorods," *J. Alloys Compd.*, vol. 644, pp. 430-437, 2015. Doi: 10.1016/j.jallcom.2015.05.078.

[12] I. W. Eltara, F. Widyawati, S. Bahtiar, and S. Hidayat, "Sintesis manganese ferrite dengan metode mechanical alloying dari bijih mangan alam," *Hexagon Jurnal Teknik dan Sains*, vol. 3, no. 1, pp. 29-33, 2022. Doi:10.36761/hexagon.v3i1.1345.

METALURGI
Majalah Ilmu dan Teknologi
p-ISSN 0126-3188 | e-ISSN 2443-3926
ejurnalmaterialmetalurgi.lipi.go.id

CHARACTERIZATION AND ANALYSIS OF HARDNESS, MICROSTRUCTURE, AND CRYSTALLOGRAPHY OF SS 304-SHEATHED MgB_2 SUPERCONDUCTING WIRES

Rizky Ramadhani Rivai[a], Andika Widya Pramono[b*], Tri Hardi Priyanto[c], Awan Maghfirah[a]

[a]Physics Study Program, University of North Sumatra
Jl. Dr. T. Mansur No. 9, Medan, Sumatera Utara, Indonesia 20222
[b]Research Center for Advanced Materials, National Research and Innovation Agency
[c]Research Center for Radiation Detection and Nuclear Analysis Technology,
National Research and Innovation Agency
B.J. Habibie Sains and Technology Area, Banten, Indonesia 15314
*E-mail: andi010@brin.go.id

Received: 07-01-2023, Revised: 27-04-2023, Accepted: 19-05-2023

Abstract

This research was conducted to analyze the hardness, microstructural morphology, and crystallography of the MgB_2 compound in the form of a SS 304-sheathed superconducting wire. MgB_2 superconducting wire with SS 304 outer sheath was manufactured using an ex-situ rolling process. The results of the Vickers hardness test with a load of 0.3 N showed the MgB_2 hardness value of 355.1 HV. The results of observations with SEM-EDS (scanning electron microscopy-energy dispersive spectroscopy) showed the agglomerations of the second phase of (Mg)B-O with various compositions due to the rolling process. There was also a longitudinal crack in the MgB_2 area due to the work-hardening phenomenon in the brittle MgB_2 solid. There were no obvious Bragg peaks in the MgB_2 phase. The detected Bragg peaks came from the austenitic (γ-Fe) of SS 304-sheath.

Keywords: *Magnesium diboride, agglomeration, FCD/TD, crystallographic texture, neutron absorption*

1. INTRODUCTION

Superconductors are materials capable of conducting electric current with zero resistivity at very low temperatures. Superconductors can conduct current even in the absence of a voltage source. This material can also act as a perfect diamagnetic material, so it can completely reject the external magnetic field as long as it is below its critical value (Hc) [1]. Magnesium diboride (MgB_2), which was discovered in 2001 by Nagamatsu et al., [2] is a metal-based superconducting material with a critical temperature (Tc) of 39 K, so that it can be used in the operational temperature range of 20-25 K in more economical cryocooler conditions. The research and development of MgB2 are expected to replace the low-temperature superconducting materials NbTi and Nb_3Sn due to the higher Tc of MgB_2. In addition, Mg is an abundant and cheaper metal resource compared to Nb, Ti, and Sn. Superconducting applications are usually used in the form of wire or tape. In this study, the process of making wire was carried out using the ex-situ powder-in-tube method. Using the ex-situ method shows more optimal results and low solid-state reaction between the stainless-steel sheath and MgB_2 which impacts the formation of oxides. Choi et al., [3] carried out a carbon doping process on MgB_2 superconducting wire using the ex-situ powder in-tube method.

This study; put ready-made MgB_2 powder with > 99% purity into stainless steel (SS) metal tubes. This study used SS 304 steel tubes which were cheaper than other metal tubes. The previous characterization also showed that the SS

DOI : 10.55981/metalurgi.694

Metalurgi is Sinta 2 Journal (https://sinta.ristekbrin.go.id/journals/detail?id=3708) accredited by Ministry of Research & Technology, Republic Indonesia

tube did not react with MgB_2 when heated [4]. Only a little research has been done to quantitatively characterize the crystallographic texture of MgB_2 superconducting wire, in addition to the frequency of publication topics that are not too high. The latest publication by Melone et al., [5] discusses the crystallographic texture of MgB_2 wire with SiC nano doping. Previously, Kováč et al., [6] discussed the anisotropy of the critical electric current (Ic) of in-situ MgB_2 in the form of bands, one of which is due to the texture of MgB_2 near the interface with the Fe, Ta, and Nb sheaths. Even further back, Song et al., [7] published articles on the anisotropy of grain morphology and crystallographic texture and their implications for the flux pinning mechanism of MgB_2 in the form of pellets, filaments, and thin films.

This research was conducted to characterize and analyze the crystallographic texture of MgB_2 in wire form, its hardness value, and microstructure morphology.

2. MATERIALS AND METHODS

MgB_2 powder with a purity > 99% was put into a SS 304 tube with an initial diameter of 6 mm. This MgB_2-containing SS 304 tube was rolled to reduce the wire diameter to 3.2 mm. Several tests were carried out on the rolled wire, including the Vickers hardness test, microstructure observation, XRD (x-ray diffraction) test, and crystallographic texture test.

In the Vickers hardness test, the cut and mounted wire samples were ground using abrasive paper numbers 40 to 2000 until the sample's surface was scratch-free. The samples were then polished using 1-micron alumina polishing fluid. The Vickers hardness test was performed using a pyramid-shaped diamond indenter. This test was carried out at five points with the same load, 0.3 N. The sample for the Vickers hardness test was also used for microstructure observation using a JEOL JSM-6390A SEM (scanning electron microscope).

For the XRD test, the wire sample was chopped or filed first to obtain a powder or flake form so that low-power x-rays can penetrate it. When a crystalline material is analyzed using XRD, the x-rays are diffracted at specific angles that depend on the spacing between the planes of atoms within the crystal lattice. Each set of planes diffracts the x-rays at a particular angle, producing a diffraction peak in the XRD pattern. The material's crystal structure can be determined by analyzing the positions and intensities of the diffraction peaks.

However, for x-rays to interact with the crystal lattice and produce diffraction peaks, the material must be powdered or flake. This is because x-rays have a limited penetration depth and are scattered in all directions when interacting with bulk material. By grinding or filing the sample into a powder or flake, the sample's surface area is significantly increased, allowing the x-rays to penetrate the material from many different directions and increasing the number of diffraction directions observed in the XRD pattern.

Increasing the number of diffraction directions is important because it provides more information about the material's crystal structure. The more diffraction directions observed, the more accurately the crystal structure can be determined, including the lattice parameters, space group, and the orientation of the crystal lattice concerning the sample surface. This information is important for understanding the material's physical properties, such as its mechanical, thermal, and electrical properties, and designing new materials with tailored properties.

XRD tests and analysis were carried out to determine the position of the Bragg peaks at a specific diffraction angle range and the percentage of elements contained in the MgB_2 superconducting wire, using the PANalytical EMPYREAN XRD test kit with Cu-Kα radiation, with a wavelength (λCu) of 1.54060 Å and a position angle between 10.0024° to 79.9684°.

Neutron diffraction is a powerful technique used to study the crystal structure of materials, particularly those that contain light elements such as hydrogen or lithium, which are difficult to analyze using x-ray diffraction. Neutron diffraction experiments are typically performed using a neutron source, such as a research reactor or a spallation source, which produces a beam of neutrons directed onto the sample.

The data from the XRD test with the PANalytical EMPYREAN instrument was then used to observe crystallographic textures with the neutron FCD/TD (four-circle diffractometer/texture diffractometer). The neutron FCD/TD (four-circle diffractometer/ texture diffractometer) is a specialized instrument used for neutron diffraction experiments. It consists of a sample stage that can rotate around four different axes, allowing the sample to be oriented in various positions concerning the neutron beam. The instrument is also equipped with detectors that can measure the intensity of the diffracted neutron beam at different angles,

which can be used to determine the crystal structure and orientation of the sample.

In a neutron diffraction experiment with the FCD/TD, the sample is first mounted onto the sample stage and oriented in a specific direction concerning the neutron beam. The neutron beam is then directed onto the sample, and the detectors detect the diffracted neutrons. By analyzing the positions and intensities of the diffracted neutron peaks, the material's crystal structure can be determined, including the positions of the atoms within the crystal lattice and the symmetry of the lattice.

In addition to determining the crystal structure, the FCD/TD can also be used to study crystallographic textures, which refer to the preferred orientation of the crystal lattice within the material. By rotating the sample stage around different axes and measuring the diffraction patterns at each orientation, it is possible to determine the preferred orientation of the crystal lattice and how it affects the material properties. This information is important for understanding the anisotropic properties of materials, such as their mechanical, thermal, and electrical properties, and for designing new materials with tailored properties.

This study used an FCD/TD (four-circle diffractometer/texture diffractometer) to determine the two-dimensional crystallographic texture of MgB_2 compounds with crystal orientation relative to the 2θ angles of the peak intensity of the XRD results. However, because FCD/TD used a neutron beam with a different wavelength (λn) than the Cu-Kα (λCu) wavelength from XRD PANalytical EMPYREAN, the 2θ angles of XRD had first to be converted to 2θ angles for FCD/ TD, using an equation based on Bragg's law:

$$\frac{\lambda_{Cu}}{\lambda_n} = \frac{\sin \theta_{Cu}}{\sin \theta_n} \quad (1)$$

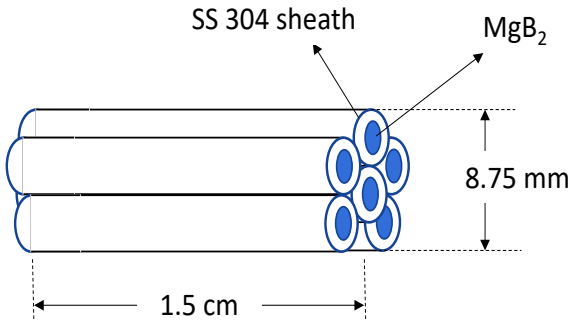

Figure 1. The bundle of MgB_2 wires

There were two types of wire samples for this neutron diffraction test, one with a diameter of 2.5 mm and the other with a diameter of 3 mm. The wire samples were bundled to provide a large enough surface area for diffraction. The average diameter of the bundled wires was 8.75 mm, with a length of 1.5 cm (Fig.1). The data resulting from neutron diffraction was then processed using the MAUD (materials analysis using diffraction) application.

3. Result and Discussion

3.1 Longitudinal Anatomy of Wire Samples

Figure 2 shows a sample of SS 304-sheathed MgB_2, which experienced a rolling reduction process. The diameter of the MgB_2 superconducting wire sample decreased from 6.0 mm to 3.2 mm, or a 71.6% reduction.

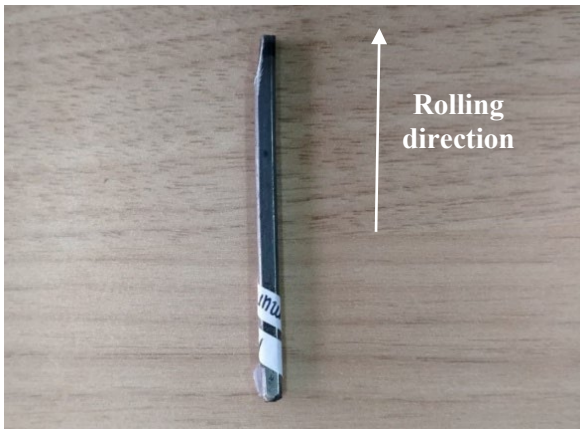

Figure 2. Sample of rolled MgB_2 superconducting wire

Figure 3 shows the longitudinal anatomy of this SS 304-sheathed MgB_2 wire sample, where the MgB_2 compound was flanked by SS 304. It can be seen that there was a longitudinal crack in the MgB_2 area due to the work-hardening phenomenon in the brittle MgB_2 solid.

Figure 4 shows the results of measuring the average thickness of the SS 304 tube and the MgB_2 area using the JEOL JSM-6390A SEM.

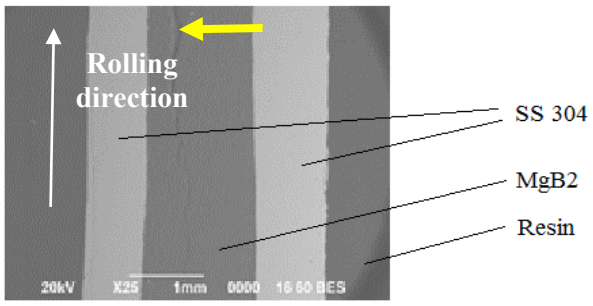

Figure 3. Longitudinal anatomy of a sample of rolled MgB_2 superconducting wire. The yellow arrow indicates the longitudinal crack in the MgB_2

Measurements of the diameter of the SS 304 wire sheath showed an average value of 3.224 mm and an inner diameter filled with MgB_2 of 1.428 mm.

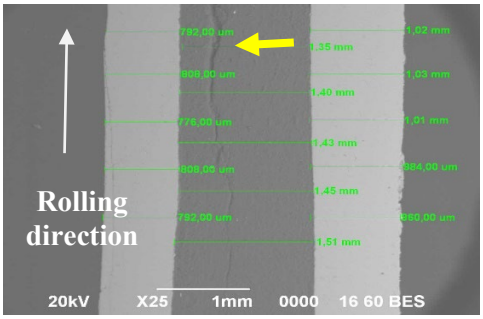

Figure 4. Measurement of the wire sample's average diameter, the thickness of the SS 304 tube, and the area of the MgB_2 compound. The yellow arrow indicates the longitudinal crack in the MgB_2

3.2 Hardness of Wire Samples

Table 1 shows the hardness value of each indentation and its average value.

Table 1. MgB_2 superconducting wire hardness values

Test No.	HV	Hardness (GPa)
1	357.8	3.5088
2	337.4	3.3087
3	317.6	3.1145
4	371.2	3.6402
5	391.5	3.8981

The Vickers hardness test took into account the value of diagonal 1 and diagonal 2 to obtain the HV hardness value using the following equation:

$$D = \frac{D1+D2}{2} \quad (2)$$

$$HV = \frac{2\,F\sin(136°/2)}{D} \quad (3)$$

$$HV = \frac{1{,}854\,F}{D^2} \quad (4)$$

where:
D = average diagonal length
D1 = length of diagonal 1
D2 = length of diagonal 2
HV = Vickers hardness value
F = load.

Based on Equations 2-4, the average hardness value of the MgB_2 superconducting wire was 355.1 HV (3.482 GPa). Previous research conducted by Herbirowo et al., [8] on SS 316-sheathed MgB_2 wire which was annealed at 800 °C and rolling, showed a hardness value of 377.2 HV. The difference in hardness values was mainly due to the nickel content in SS 304 and SS 316. SS 304 contains an average of 8.0% nickel, while SS 316 contains 10.0% nickel. The higher the nickel is, the value of the strength and hardness of the steel increases. In addition, SS 316 contains 2.0% Mo (molybdenum). Mo functions not only to increase corrosion resistance but also to increase steel's hardness, toughness, and strength.

3.3 Microstructures of MgB_2 Wire

Figure 5 shows the morphology of the MgB_2 compound on a superconducting wire. Clumping or agglomeration (white arrows) occurred in the MgB_2 compound due to the rolling process, where the MgB_2 powder wire was subjected to roll compaction pressure. The inhomogeneity of agglomerate sizes in MgB_2 powder was determined by several factors, such as the outer and inner diameters of the wire, the rolling or rolling tool system, and the interaction between process parameters and the physical properties of the material (MgB_2 and SS 304 sheath) [9].

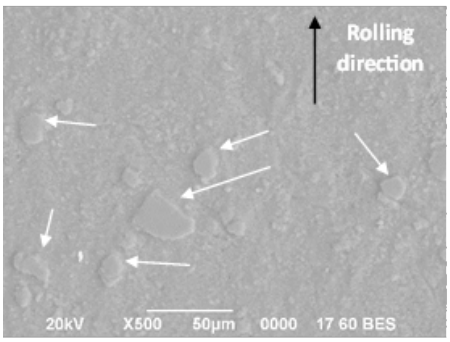

Figure 5. Morphology of MgB_2 compounds in superconducting wire samples. Agglomerations with non-uniform size distribution are indicated by white arrows

EDS analysis of these lumps also indicated the presence of the second phase (Mg)B-O (discussed later). At the same spot as Fig. 5, an elemental mapping analysis was carried out to determine the distribution of the main elements, as shown in Fig. 6.

From Figure 6, it can be seen that the most dominant elements were Mg (Fig. 6(d)), then O (Fig. 6(c)), and B (Fig. 6(b)). The presence of elemental oxygen indicated the occurrence of an oxide phase. Figure 7 shows the results of the analysis of the EDS *in-situ* composition by spot on several lumps or agglomerates. These lumps were suspected to be the second phase (Mg)B-O with various compositions (Figs. 7(a)-(c), and (e)).

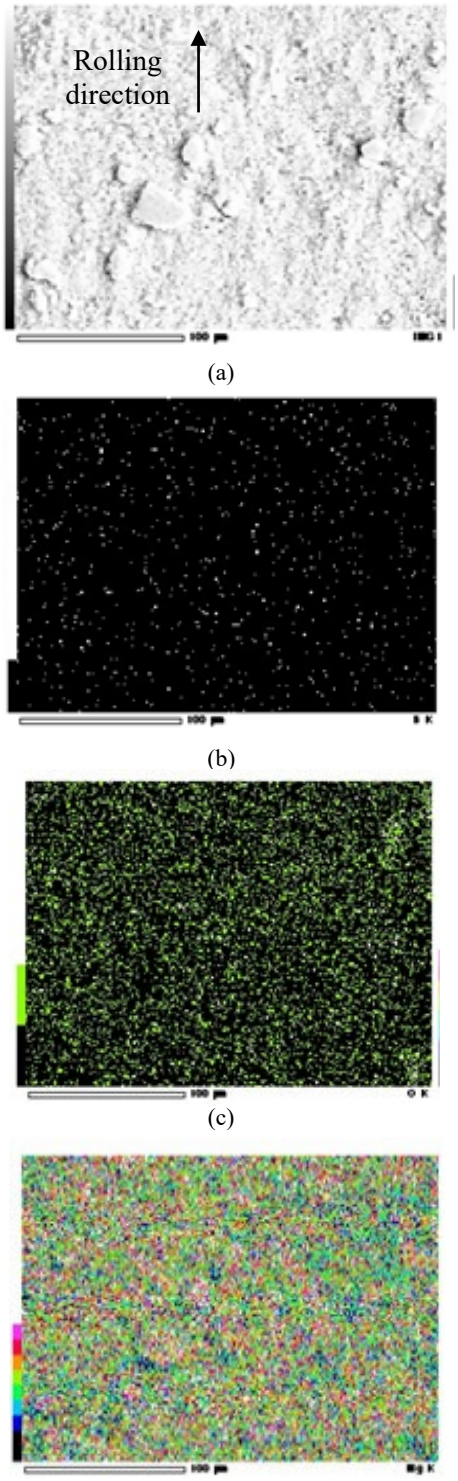

Figure 6. Results of elemental mapping analysis on MgB_2 superconducting wire samples: (a) SEM, (b) elemental boron (B) (c) elemental oxygen (O), and (d) elemental magnesium (Mg)

The existence of the second phase (Mg)B-O was also previously reported by Chen et al., [10], where the element oxygen originated from the boron powder precursor, B_2O_3.

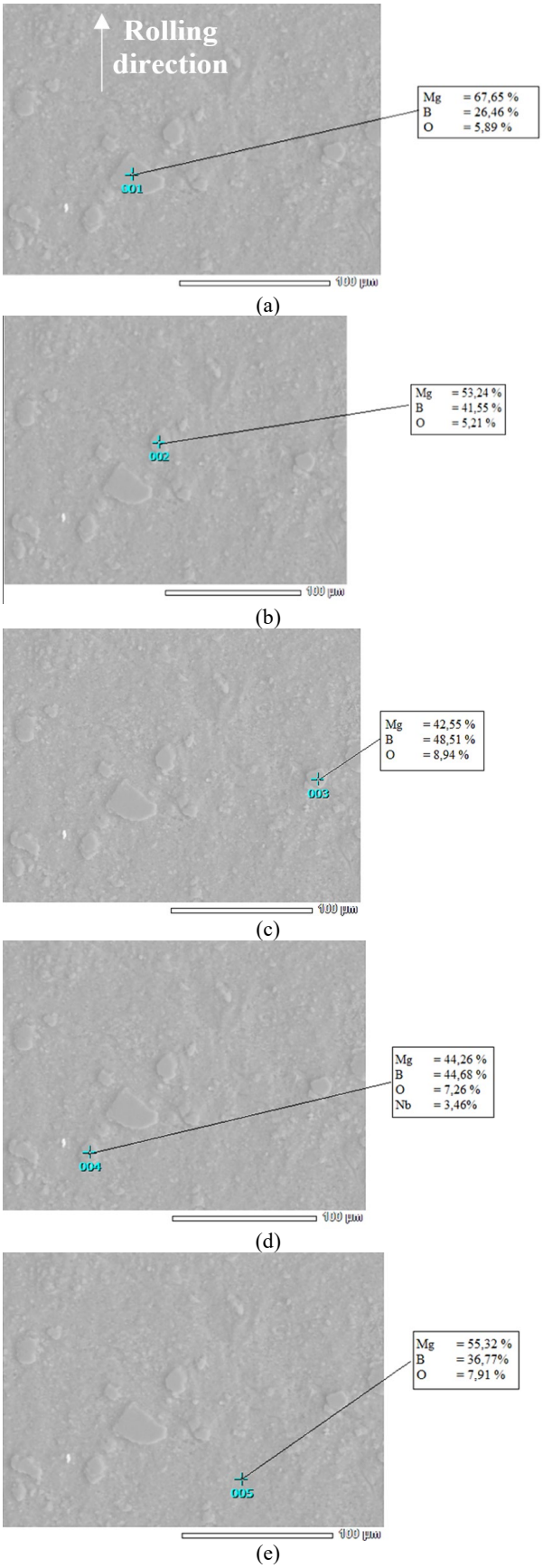

Figure 7. The EDS in-situ composition analysis results by spot on the agglomerates of the MgB_2 compound indicated the presence of a second phase (Mg)BO with various composition variations

Amorphous boron contains more B_2O_3 compounds than crystalline boron. However, after synthesis, the second phase (Mg)B-O is mainly produced by crystalline boron [10]. The results of the EDS analysis of the agglomerates in Fig. 7(d) show the presence of Nb (niobium) impurity.

3.4 X-Ray Diffraction Analysis

Figure 8 shows the XRD results of the MgB_2 superconducting wire sample, where the highest peak of the MgB_2 compound occurs at an angle of $2\theta = 42.428°$ and for iron (Fe) from the SS 304 sheath at 44.510°. The compositional analysis of the XRD results showed an MgB_2 content of 74.1% and α iron of 25.9%.

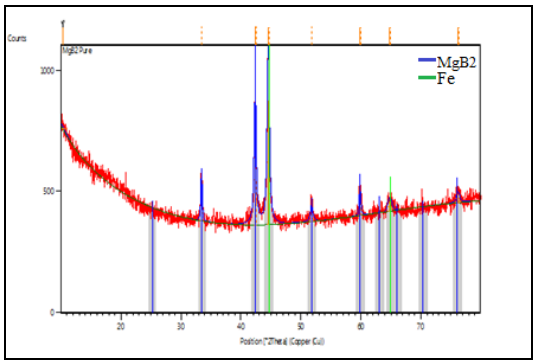

Figure 8. Graph of XRD characterization results of MgB_2 superconducting wire

3.5 Crystallography Analysis

Previously it was known that the maximum intensity of MgB_2 occurred at an angle of $2\theta_{Cu} = 42.428°$ or $\theta_{Cu} = 21.214°$. By using the values of $\lambda_{Cu} = 1.54060$ Å and $\lambda_n = 1.2799$ Å and Equation 1, the value of the angle θ_n was calculated to be 17.495°, or $2\theta_n = 34.989°$. The results of the diffraction data from FCD/TD were then processed in the MAUD (material analysis using diffraction) application.

Two types of phases were observed using FCD/TD, namely γ-Fe (austenite) and MgB_2. Austenitic steel hasana fcc (face-centered cubic) structure with a space group of Fm-3m. Depending on the carbon content, the lattice parameter of γ-Fe varies from 3.5680 Å (C = 0.45%) to 3.6043 Å (C = 1.25%) [11]. MgB_2 has a hexagonal structure with lattice parameters a = b = 3.06 Å c= 3.52 Å, α = 90°, β = 90°, γ = 120,° and a space group of P6/mmm [12]-[13].

From the results of the initial analysis of the Bragg peak with MAUD, there was good compatibility between the Bragg peaks of the austenitic γ-Fe phase with the experimental results, as shown in Fig. 9 (for wire diameter = 3.0 mm) and Fig. 10 (for wire diameter = 2.5 mm).

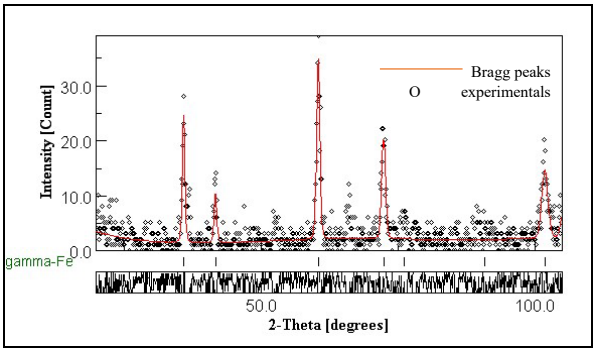

Figure 9. The compatibility between γ-Fe phase Bragg peaks with the experimental results, for wire diameter = 3.0 mm

The difference in peak intensities in Fig. 9 and Fig. 10 can be correlated with the extent of wire reduction. The wire reduction was 75.0% for a wire diameter of 3.0 mm, whereas the wire reduction was 82.6% for a wire diameter of 2.5 mm. Such wire reduction induced the development of crystallographic texture or preferred orientations due to material deformation [13]-[14].

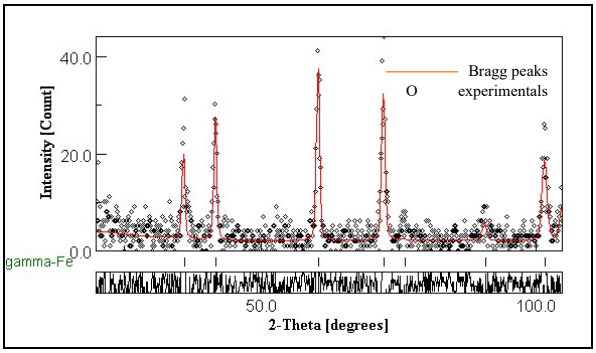

Figure 10. The compatibility between γ-Fe phase Bragg peaks with the experimental results, for wire diameter = 2.5 mm

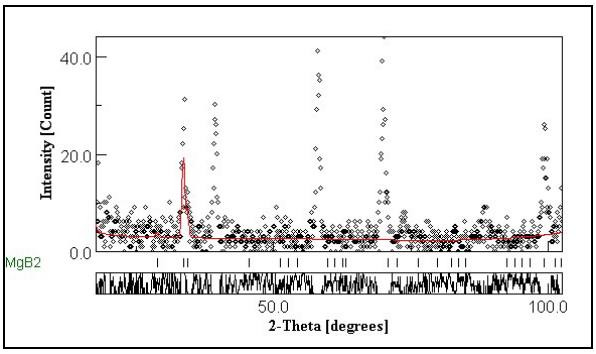

Figure 11. No compatibility between MgB_2 Bragg peaks with the experimental results, for wire diameter = 3.0 mm

In the MgB_2 phase, there was no Bragg peak corresponding to the theoretically produced MgB_2 Miller index for both wires with diameters

of 2.5 mm and 3.0 mm (Figs. 11 and 12). There is no Bragg peak in the MgB_2 diffraction pattern since boron, and its boride compound are neutron-absorbing materials [15]-[16]. Even though the abundance of ^{10}B isotope in nature is only 18.9-20.4% [17], it has a neutron cross-section of 3835-3840 barns (1 barn = $10^{-24}cm^2$) for 0.025 eV neutron [18]. On the other hand, the ^{11}B isotope (with the 79.6-81.1% portion) has a neutron cross-section of only 5.28 barns [18]-[19].

To overcome this issue, researchers may use other techniques such as neutron diffraction, which is more sensitive to the presence of ^{10}B, or use isotopically enriched samples containing a higher proportion of ^{11}B. These methods can help to improve the resolution and accuracy of the XRD analysis of MgB_2.

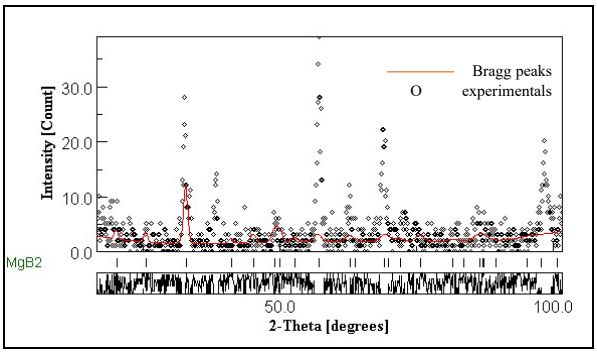

Figure 12. No compatibility between MgB_2 Bragg peaks with the experimental results, for wire diameter = 2.5 mm

4. CONCLUSION

The average hardness value of the MgB_2-SS 304 superconducting wire was 355.1 HV (3.482 GPa), lower than that of the MgB_2-SS 316 superconducting wire. This condition was triggered by the higher Ni and Mo content in SS 316 compared to SS 304. Observation of the microstructure of the MgB_2 compound on this superconducting wire shows the presence of agglomerates of various sizes, which were also the second (Mg)B-O phase with variations in composition. There were no obvious Bragg peaks in the MgB_2 phase. This was probably due to the effect of the very large neutron absorption cross-section of the ^{10}B isotope so that most of the neutrons were absorbed by the material, and only a small part of neutrons was scattered and captured by the detector. The detected Bragg peaks came from the austenitic (γ-Fe) of SS 304-sheath.

ACKNOWLEDGMENT

The authors would like to thank and appreciate the neutron scattering laboratory of the Research Center for Radiation Detection and Nuclear Analysis Technology and the ferrous materials research group of the Research Center for Metallurgy, National Research and Innovation Agency of Indonesia for their scientific and technical supports so that samples and neutron-diffraction data can be obtained.

REFERENCES

[1] N. Nurmalita, N. Amani, and F. Fauzi, "XRD analysis of Bi-2212 superconductors prepared by the self-flux method," *Jurnal Natural*, vol. 13, no. 1, pp. 23-27, 2013. Doi:10.24815/jn.v13i1.841

[2] Y. P. Sun, W. H. Song, J. M. Dai, B. Zhao, J. J. Du, H. H. Wen, and Z. X. Zhao, "Superconductivity at 49 K in copper doping magnesium diboride," *arXiv preprint cond-mat/0103101*, 2001.

[3] S. Choi, D. Patel, J. H. Kim, H. Kumakura, A. Matsumoto, G. Nishijima, S. H. Kim, J. Joo, and M. Maeda, "Evaluation and control of residual amorphous phases in carbon-doped MgB_2 superconductors," *J. Alloys Compd.*, vol. 864, pp. 158867, 2021. Doi:10.1016/j.jallcom.2021.158867.

[4] S. Herbirowo, M. N. Hanafi, A. Imaduddin, E. P. Utomo, Hendrik, A. Trenggono, and E. Yustanti, "Pengaruh doping nikel dan suhu sinter pada pembuatan kawat superkonduktor magnesium diborida," *Indonesian Journal of Applied Physics*, vol. 10, no. 2, pp. 116-125, 2020.

[5] M. Melone, M. Moran, F. Malamud, M. T. Malachevsky, and A. Serquis, "Crystallographic texture study of nano-SiC-doped MgB_2 wires," *IEEE Transactions on Applied Superconductivity*, vol. 31, no. 5, pp. 1-5, 2021. Doi: 10.1109/TASC.2021.3068088.

[6] P. Kováč, T. Melišek, and I. Hušek, "Ic anisotropy of in situ made MgB_2 tapes," *Supercond Sci Technol*, vol. 18, no. 7, pp. L45-L48, 2005. Doi:10.1088/0953-2048/18/7/L02.

[7] X. Song, S. E. Babcock, C. B. Eom, D. C. Larbalestier, K. A. Regan, R. J. Cava, S. L. Bud'Ko, P. C. Canfield, and D. K. Finnemore, "Anisotropic grain morphology, crystallographic texture and their implications for flux pinning mechanisms in MgB_2 pellets, filaments, and thin films," *Supercond Sci Technol*, vol. 15, no. 4, pp. 511-518, 2002. Doi: 10.1088/0953-2048/15/4/306.

[8] S. Herbirowo, V. Puspasari, H. Nugraha, E. Sulistiyo, A. W. Pramono, and A. Imaduddin, "Fabrikasi kawat resistansi nol

berbahan MgB2/stainless steel dengan variasi reduksi ukuran melalui pengerolan dingin terhadap karakteristik mekanik dan struktur mikro," *Energi & Kelistrikan*, vol. 13, no. 2, pp. 242-249, 2021. Doi: 10.33322/energi.v13i2.1491.

[9] L. P. Gandarillas, A. P. Gago, A. Mazor, P. Kleinebudde, O. Lecoq, and A. Michrafy, "Effect of roll-compaction and milling conditions on granules and tablet properties," *European Journal of Pharmaceutics and Biopharmaceutics*, vol. 106, pp. 38-49, 2016. Doi: 10.1016/j.ejpb.2016.05.020.

[10] S. K. Chen, K. A. Yates, M. G. Blamire, and J. L. M. Driscoll, "Strong influence of boron precursor powder on the critical current density of MgB_2," *Supercond Sci Technol*, vol. 18, no. 11, pp. 1473-1477, 2005. Doi:10.1088/0953-2048/18/11/011.

[11] J. Mazur, "Lattice parameters of martensite and austenite," *Nature*, vol. 166, no. 4228, pp. 828-828, 1950. Doi: 10.1038/166828a0.

[12] A. Jain, S. P. Ong, G. Hautier, W. Chen, W. D. Richards, S. Dacek, S. Cholia, D. Gunter, D. Skinner, G. Ceder, and K. A. Persson, "Commentary: The materials project: a materials genome approach to accelerating materials innovation," *APL Mater*, vol. 1, no. 1, pp. 011002, 2013. Doi: 10.1063/1.4812323.

[13] S. T. Faris, "Analysis of plane strain rolling rigid plastic materials using finite element method," *Diyala Journal of Engineering Sciences*, vol. 8, no. 2, pp. 99-115, 2015. Doi:10.24237/djes.2015.08208.

[14] A. Pramono and J. Bouffette, *Pengantar tekstur kristalografi: teori dan aplikasi*. LIPI Press, 2022. Doi:10.14203/press.393.

[15] I. Hore-Lacy, "Nuclear Power," *Nuclear Energy in the 21st Century*, pp. 37-53, 2007. Doi:10.1016/B978-012373622-2/50006-4.

[16] "Neutron Absorber - an overview | ScienceDirect Topics." https://www.sciencedirect.com/topics/earth-and-planetary-sciences/neutron-absorber (accessed Jan. 03, 2023).

[17] S. Barth, "Boron isotopic analysis of natural fresh and saline waters by negative thermal ionization mass spectrometry," *Chem Geol*, vol. 143, no. 3-4, pp. 255-261, 1997. Doi:10.1016/S0009-2541(97)00107-1.

[18] N. Soppera, M. Bossant, O. Cabellos, E. Dupont, and C. J. Díez, "Janis: NEA java-based nuclear data information system," *EPJ Web Conf*, vol. 146, pp. 07006, 2017. Doi:10.1051/epjconf/201714607006.

[19] E. C. Auden, H. M. Quinn, S. A. Wender, J. M. O'Donnell, P. W. Lisowski, J. S. George, N. Xu, D. A. Black, and J. D. Black, "Thermal neutron-induced single-event upsets in microcontrollers containing boron-10," *IEEE Trans Nucl Sci*, vol. 67, no. 1, pp. 29-37, 2020. Doi: 10.1109/TNS.2019.2951996.

METALURGI
Majalah Ilmu dan Teknologi
p-ISSN 0126-3188 | e-ISSN 2443-3926
ejurnalmaterialmetalurgi.lipi.go.id

A PRELIMINARY STUDY OF COBALT SOLVENT EXTRACTION FROM NICKEL SULPHATE SOLUTION USING ORGANIC EXTRACTANT-PC-88A

Arief Dwi Rohman[a,*], Rudi Subagja[b], Anistasia Milandia[a], Soesaptri Oediyani[a], Iwan Setiawan[b]

[a]Metallurgical Engineering, Sultan Ageng Tirtayasa University
Jl. Jenderal Sudirman Km 3, Cilegon, Banten, Indonesia 42435
[b]Research Centre for Metallurgy, National Research and Innovation Agency
B.J. Habibie Sains and Technology Area, Banten, Indonesia 15314
*E-mail: adwi7108@gmail.com

Received: 10-10-2022, Revised: 10-05-2023, Accepted: 19-05-2023

Abstract

In the present study, a solvent extraction experiment was done to separate cobalt from the nickel sulfate solution using 2-ethylhexyl phosphonic acid mono-2-ethylhexyl ester (PC-88A) as an extractant. The experiment was carried out on a laboratory scale using a separating funnel to extract cobalt from the nickel sulfate solution with PC-88A. The mixed solution was shaken in a separating funnel for a specified time. After the solvent extraction experiment was finished, the organic phase PC-88A was separated from the nickel sulfate solution by decantation. The nickel and cobalt content in the aqueous nickel sulfate solution was then analyzed using AAS (atomic absorption spectrophotometry). In this experiment, the variable for experiments was covering solution pH from 2 to 6, shaking time from 30 minutes to 120 minutes, shaking speed from 20 rpm (revolutions per minute) to 80 rpm, and the volume ratio of aqueous to organic phase (A:O ratio) was from 1:1 to 1:4. The effects that experimental variables to the cobalt extraction were observed in this experiment. The result of the experiment at room temperature, solution pH 5, shaking speed 60 rpm, shaking time 90 minutes, A:O ratio 1:4 and concentration of PC- 88A 40% show PC-88A can extract 97.21% of cobalt from nickel sulfate solution. Therefore, it was necessary to conduct two stage extraction process to extract 100% of the cobalt from the nickel sulfate solution.

Keywords: *Solvent extraction, nickel, cobalt, nickel sulphate, PC-88A*

1. INTRODUCTION

Nickel and cobalt are used extensively in metallurgy and non-metallurgy. There are many uses for nickel, such as stainless steel, high-temperature steel, magnetic materials, electroplating, non-ferrous alloys, ceramic materials, catalysts, batteries, fuel cells, and chemicals [1]-[2]. There are numerous applications for cobalt in the metallurgical, petroleum, chemical, electronic, pharmaceutical, and medical industries because of its unique chemical and physical properties. Cobalt is commonly used in the metallurgical industry to produce alloy metals for gas turbines, nuclear power plants, engine vanes, automotive engines, engine valves, aviation fuel nozzles, and cutting wear-resistant tools [3]-[5], magnetic materials such as Alnico and Samarium cobalt [6]-[8], the catalyst for sulfur removal and oil hydrogenation processes [9]-[11], drying materials for paint, promoters for the polymerization process [12], pigment materials [13]-[14], raw materials for rechargeable batteries [15], Fuel Cell Cathode materials [16], and implant materials for heap joints, dentist, cardiovascular stent [17]-[21]. Cobalt has a broad spectrum application in many industries; therefore cobalt consumption in the world tends to increase [22]. There are predictions that global cobalt consumption will reach 220 000 tons by 2025 and 390 000 tons by 2030 [23].

Cobalt is generally obtained as a by-product of the nickel, copper, and zinc extraction process

DOI : 10.55981/metalurgi.684

Metalurgi is Sinta 2 Journal (https://sinta.ristekbrin.go.id/journals/detail?id=3708) accredited by Ministry of Research & Technology, Republic Indonesia

[22], [24]-[29] and from used batteries [30]-[31]. Cobalt can also be obtained from the nickel matte [32]-[33] by-product of nickel laterite processing through the caron process or HPAL (high-pressure acid leaching) [1]. In this process, cobalt is obtained through the leaching process of materials containing cobalt, followed by a solvent extraction process to separate the cobalt from other contained elements in the solution and the cobalt deposition process from the solution, including the electrowinning process to precipitate the cobalt from the cobalt chloride solutions [34].

Solvent extraction separate a metal ion from another existing metal ion in a solution (water phase) by adding insoluble organic materials into the water phase to transfer a metal ion from the water phase to the organic phase. The stripping process is carried out to remove the loaded metal from the organic phase. Metals can be separated from complex ions in solutions by solvent extraction because it is an efficient and flexible method [35].

The are many extractants for the cobalt solvent extraction process. The extractants used are Cyanex 272, D2EHPA (acid extractant), Alamine 306, Alamine 304 (base extractant), and Cyanex 923 (solvating extractant). In acidic solutions, Cyanex 272 and D2EHPA have been used to extract cobalt, but when the solution contains ionic manganese, these two extractants are less effective at extracting cobalt, as they can both extract manganese first before extracting cobalt [36]; therefore, alternative extractants are needed for cobalt extraction from nickel sulfate solution.

To separate cobalt from the nickel sulfate solution in this paper, a solvent extraction study has been done by using PC-88A as an organic extractant. This study aims to investigate the effect of solvent extraction parameters, such as shaking speed, shaking time, water phase to organic phase ratio, and solution pH, on cobalt extraction.

2. MATERIALS AND METHODS

2.1 Raw Materials for Experiment

The raw material for this experiment was a nickel sulfate solution containing cobalt ions. To obtain this mixed solution, nickel sulfate hexahydrate (Merck) and cobalt sulfate heptahydrate (Pudak Scientific) were dissolved in H_2SO_4 (aqueous sulfuric acid) solution and mixed to form a nickel-cobalt sulfate solution with an approximately 10: 0.5 Ni/Co mass ratio. In contrast the organic extractant used in the experiment was 2-ethythexyl phosphonic acid mono-2-ethylhexyl, known with the trade name PC-88A from Daihachi Chemical. In some experiments, PC-88A was diluted with kerosene to obtain an appropriate PC-88A concentration for the solvent extraction. The detail of the PC-88A Kerosine volume ratio is explained in the section variable for an experiment.

2.2 Variable for Experiment

The variables covered in this solvent extraction experiment were shaking speed 20; 40; 60; 80 rpm, shaking time 30; 45; 60; 90; 120 minutes, a ratio of water to organic phase (A:O ratio) 1:2; 1:3; 1:4, the concentration of PC88A 20, 40, 60, 80, 100%, and pH adjusted with sulfuric acid or sodium hydroxide solutions. Those experimental variables were observed in the cobalt extraction from the nickel sulfate solution by PC-88A.

2.3 Solvent Extraction Experiment

The solvent extraction experiment to extract cobalt from the nickel sulfate-containing ionic cobalt solution (water phase) was carried out by mixing a certain volume of nickel sulfate solution (water phase) with PC-88A (organic phase) in the separating funnel. The mixed solution was shaken for a certain time using a mechanical shaker. After the experiment, the organic phase and the aqueous phase were separated by decantation, and the solution's nickel and cobalt content was then determined using an AAS (atomic absorption spectrophotometry). The percentage of cobalt extraction was calculated using Equation 1.

$$\%\, E_{Co} = \frac{[Co]_I - [Co]_A}{[Co]_I} \times 100\ \% \qquad (1)$$

Some ionic nickel may be removed from the sulfate solution during the cobalt extraction. As a result, Equation 2 is utilized to determine the percentage of nickel extraction.

$$\%\, E_{Ni} = \frac{[Ni]_I - [Ni]_A}{[Ni]_I} \times 100\ \% \qquad (2)$$

Where:

$\%\, E_{Co}$ = Cobalt percent extraction
$\%\, E_{Ni}$ = Nickel percent extraction
$[Co]_I$ = Cobalt content in the nickel sulfate solution before extraction
$[Co]_A$ = Cobalt content in the nickel sulfate solution after extraction
$[Ni]_I$ = Nickel content in the nickel sulfate solution before extraction
$[Ni]_A$ = Nickel content in the nickel sulfate solution after extraction

3. Result and Discussion

3.1 Effect of Shaking Speed on Cobalt Extraction

The effect of shaking speed on a cobalt extraction from a nickel sulfate solution containing cobalt ions was studied at room temperature, the shaking time was 30 minutes, the water-to-organic phase ratio was 1:1, and the solution pH was 2 and 5, and shaking speed was 20 rpm, 40 rpm, 60 rpm, and 80 rpm. The result of an experiment in Fig. 1 shows that increasing in shaking speed from 20 rpm to 40 rpm caused a slight increase in the nickel and cobalt extraction, but a further increase in rpm to 80 rpm had not given any significant effect for both cobalt and nickel extractions. This experiment result shows the minimum shaking speed for creating a good contact between organic phase and aqueous phase was at 40 rpm. For shaking speed equal to 40 rpm or longer than 40 rpm, interfacial contact between organic and water phases has been effective for the cobalt transferring process from the water phase to the organic phase. Another research activity show the same tendency during cobalt extraction from nickel chloride solution by using TNOA (tri normal octyl amine) as an organic extractant [37].

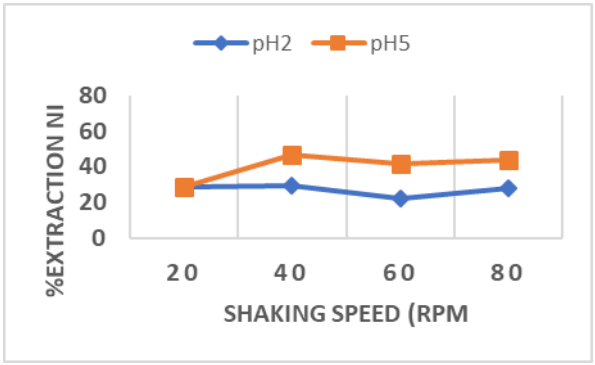

(a)

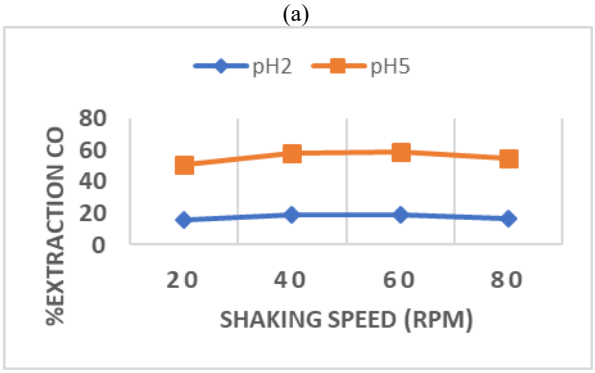

(b)

Figure 1. Effect of shaking speed on metal extraction, (a) Ni Extraction, and (b) Co extraction

3.2 Effect of Shaking Time on Cobalt Extraction

The effect of shaking time on a cobalt and nickel extraction from the nickel sulfate solution containing cobalt ions was investigated at room temperature, with the solution pH ranging between 2 and 5, the volume water to organic phase ratio (A:O ratio) was set to 1:1. The shaking time ranged from 30 minutes to 120 minutes. The results of an experiment are shown in Fig. 2, which demonstrates that increasing the shaking time from 30 minutes to 120 minutes had little effect on the extraction of nickel and cobalt. The experiment's findings indicate that 30 minutes of shaking was the minimum amount of shaking required to transfer cobalt from the water phase to the organic phase. The aqueous and organic phases have been thoroughly mixed for 30 minutes or more of shaking, and the cobalt transfer process is more effective now. The same pattern was seen in a different research project that used TNOA (tri-normal-octyl-amine) as an organic extractant for extracting cobalt from a nickel chloride solution [37].

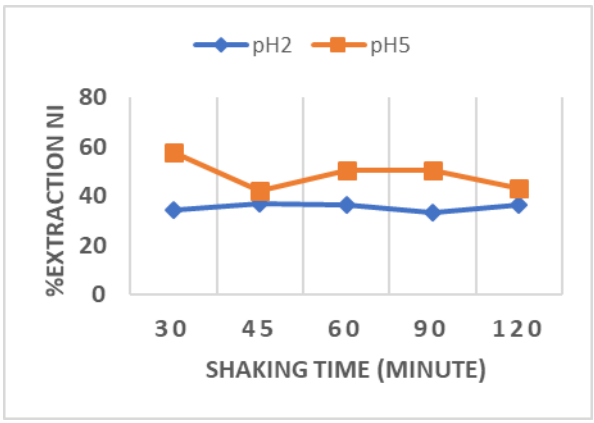

(a)

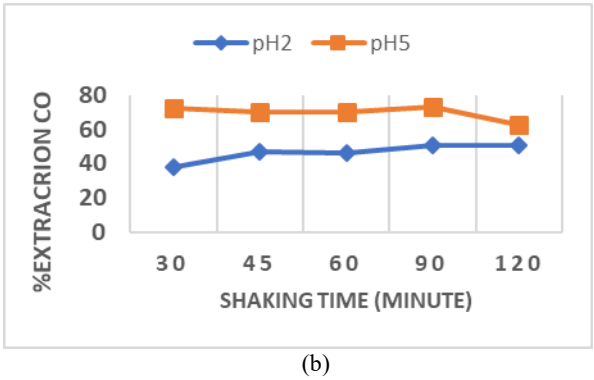

(b)

Figure 2. Shaking time effect on nickel and cobalt extraction, (a) Ni, and (b) Co

3.3 Effect of A:O ratio on Cobalt Extraction

This experiment examined the role of the aqueous to organic phases (A:O) ratio on the

extraction of cobalt and nickel from a nickel sulfate solution containing cobalt ions. The experiment was conducted at room temperature, with the solution's pH range being between 2 and 5, shaking time for 90 minutes, and the A:O ratio varying from 1:1 to 1:4. The experimental results in Fig. 3 show that the percentage of cobalt extraction increases as the A:O ratio increases in all solution pH conditions, due to the increased PC-88A concentration, which encourages cobalt extraction and causes the cobalt extraction from nickel sulfate solution to increase. A higher percentage of cobalt extraction was attained in the solution with an A:O ratio of 1:4 due to the higher PC-88A content, which promotes cobalt extraction.

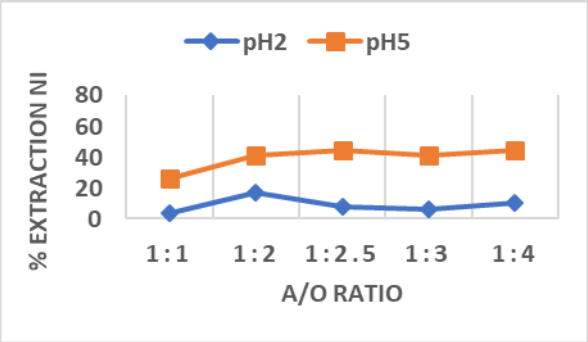

(a)

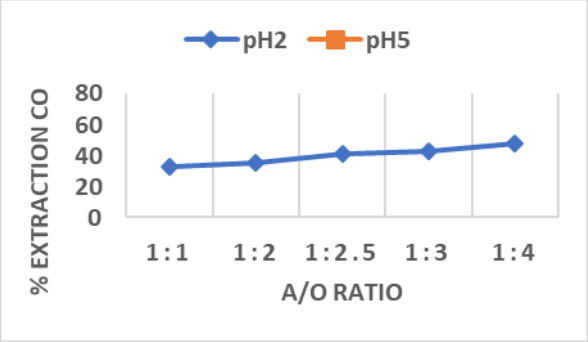

(b)

Figure 3. Effect of (A:O) ratio on metal extraction (a) Ni, and (b) Co

The results of the experiment also show that 87.97 % of cobalt and 57 % of nickel was extracted by the PC-88A from the nickel sulfate solution at a solution pH 5 and an A:O ratio equal to 1:4. Comparing our result with another research activity, there is similar tendency with Julian wang [38] experimental result which had conducted a research activity to separate cobalt from nickel sulfate solutions. His experiment result shows the cobalt extraction from the sulfate solution increased when the ratio of the organic phase to the aqueous phase was increased. These experiment results show the increase of the A:O ratio creates more concentration of extractant in the solution which creates more cobalt extraction.

3.4 Effect of PC 88A Concentration on Cobalt Extraction

The effect of PC-88A concentration on cobalt extraction from the nickel sulfate solution containing cobalt ions was examined at room temperature, with the solution pH ranging between 2 and 5, shaking time was 90 minutes, shaking speed was 60 rpm, A:O ratio was 1:4, and PC 88A concentration varied from 20% to 100%.

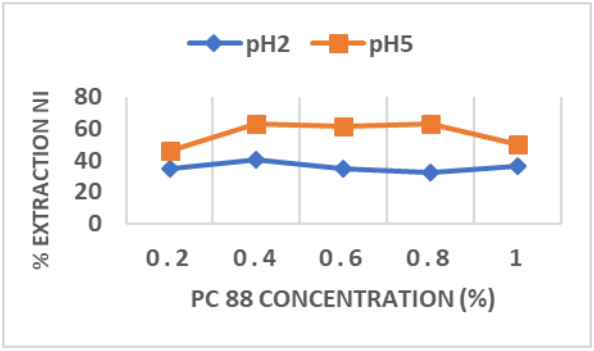

(a)

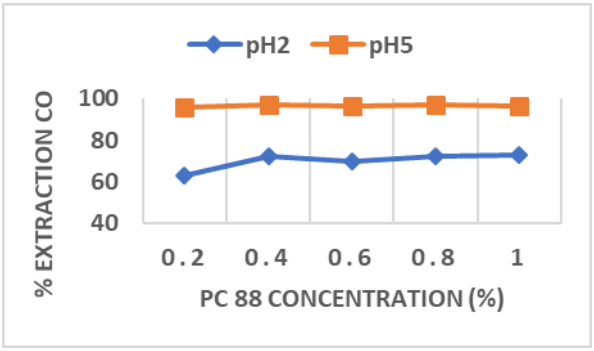

(b)

Figure 4. Effect of PC 88A concentration on metal extraction (a) Ni, and (b) Co

The experimental results in Fig. 4 demonstrate that increasing the concentration of PC 88A from 20% to 40% resulted in a slight increase in the extraction of nickel and cobalt, but increasing the concentration of PC 88A from 40% to 100% has had no significant effect on the extraction of nickel and cobalt. As shown by the experiment's findings in Fig. 4, adding PC 88A had less impact on cobalt extraction than raising the solution pH from 2 to 5. Cobalt exists as a cation species in the solution phase, responsible for the increased cobalt extraction at a higher solution pH [39], which is easier to extract by acidic organophosphorus extractant PC-88A [40].

3.5 Effect of Solution pH on Cobalt Extraction

The effect of solution pH on the nickel and cobalt extraction from nickel sulfate solution containing cobalt ions was studied at room temperature, the PC-88A concentration was 40%, and the solution pH was varied from pH 2 to pH 6. The experimental results in Fig. 5 show that increasing the solution pH from pH 2 to pH 5 causes an increasing in cobalt and nickel extraction. Referring to Equation 3, when the water phase (nickel sulfate solution) is mixed with the organic phase (PC-88A), the ionic cobalt (Co^{2+}) in the nickel sulfate solution reacts with the organic phase of PC-88A (RH) according to the following the reaction:

$$Co^{2+} + 2\,RH = R_2Co + 2\,H^+ \quad (3)$$

The equilibrium constant (K) for reaction 3 is expressed by Equation 4 as follows:

$$K = \frac{[R_2Co][H^+]^2}{[Co^{2+}][RH]^2} \quad (4)$$

And if the cobalt distribution in the organic phase (R_2C_O) and the water phase (Co^{2+}) is expressed by Equation 5 below:

$$D = [R_2Co]/[Co^{2+}] \quad (5)$$

Then Equation 5 is substituted into Equation 4, the equilibrium constant of Equation 3 can be expressed by Equation 6 as follows:

$$K = \frac{D\,[H^+]^2}{[RH]^2} \quad (6)$$

And if Equation 6 is expressed in logarithmic form it will creates Equation 7 as follows:

$$\text{Log } D = \log K + 2 \log RH + 2\,pH \quad (7)$$

Equation 7 shows the increase of pH could increase the cobalt distribution in the organic phase, or the cobalt extraction increases when the solution pH increases. The correlation between pH and with a distribution of cobalt in organic phase (D) in Equation 7 has the same tendencies and with the experimental results in Fig. 5. Another experiment conducted by Julian [38] and Luiz [39] show the same tendencies. Luiz conducted experimented to separate cobalt and nickel from spent nickel–metal–hydride batteries by solvent extraction with D2EHPA (di-2-ethylhexyl phosphoric acid) followed by Cyanex 272 (bis-2,4,4-trimethylpentyl phosphinic acid, and Junlian [38] conducted an experiment to separate cobalt and nickel separation from sulfate solutions by using (2-ethylhexyl) (2,4,4-trimethylpentyl) phosphinic acid. Their experiment result shows the cobalt and nickel extraction increased when the solution pH increased. Another similar results are observed by Luo, who conducted experiments on cobalt extraction from chloride solution with PC-88A as an extractant, where an increase in the pH of the solution led to an increase in cobalt extraction [41].

3.6 Multistage Extraction using McCabe Thiele Method

The experimental result in Fig. 5 reveals that the maximum value of cobalt extraction with PC 88 A is 97,21% at pH 5. As a result, some cobalt ions remain in the nickel sulfate solution. A multi-stage solvent extraction procedure should be used to obtain more pure nickel sulfate solutions. A cobalt-free nickel sulfate solution is created at this stage.

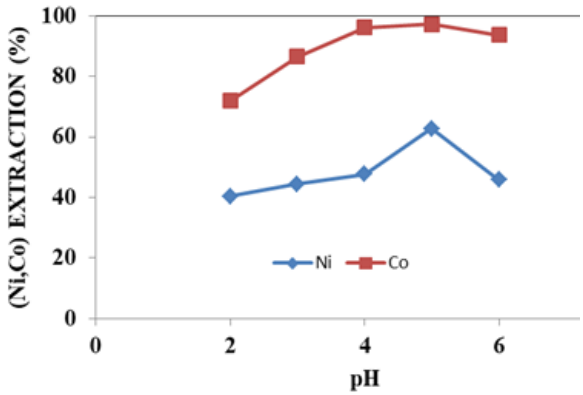

Figure 5. Effect of pH on cobalt and nickel extraction

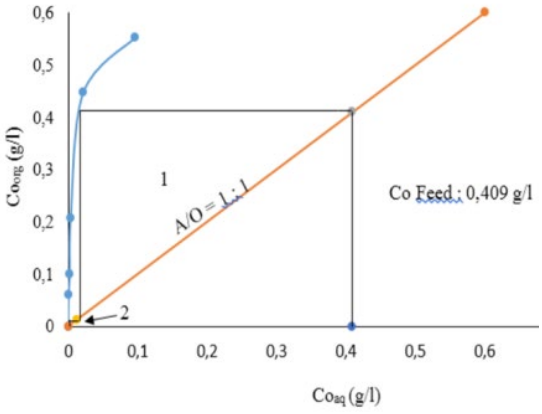

Figure 6. Mc Cabe thiele diagram use for the extraction process of Co from nickel sulfate

In this study, the McCabe Thiele diagram was used for the multistage extraction simulation, as it is depicted in Fig. 6, where the raw material used was a nickel sulfate solution with a nickel content of 8.775 g/l and cobalt content of 0.409 g/l. This solution composition has been used in previous research to observe the effect of pH, PC 88A concentration, shaking speed, shaking time, and aqueous-to-organic ratio on cobalt extraction. The McCabe Thiele diagram in Fig. 6 shows two stages. The extraction process can separate all the cobalt ions from the nickel sulfate solution using a 40% concentration of PC-88A extractant. In the first extraction stage, it produces a nickel sulfate solution (water phase) containing 0.0114 g/L cobalt ions, and in the second.

4. CONCLUSION

The conclusion of the study on the separation of cobalt from nickel sulfate solution containing cobalt ions using the solvent extraction methods is cobalt ion can be separated from nickel sulfate solution containing cobalt ion by solvent extraction method using organic solvent PC-88A. The best condition for cobalt extraction from nickel sulfate solutions is at room temperature, solution pH 5, shaking speed 60 rpm, shaking time 90 minutes, A:O ratio of 1:4 with a PC-88A concentration of 40 %. At this condition almost 97.21 % of Cobalt could be extracted from the nickel sulfate solutions. Therefore, the 2-stage extraction process with PC-88A is needed to obtain a more purer nickel sulfate solution.

ACKNOWLEDGMENT

The authors wish to acknowledge The Research centre for Metallurgy of the National Innovation Research Agency-Indonesia for the Research facilities and financial support in conducting the research activity. Furthermore we thank Mr. Januar Ibrahim for his support in chemical analysis.

REFERENCES

[1] A. D. Dalvi, W. G. Bacon, and R. C. Osborne, "The past and the future of nickel laterites world's land based nickel resources and primary nickel production," *PDAC 2004 Int. Conv.*, pp. 1-27, 2004.

[2] A. Nieto, V. Montaruli, and M. Cardu, "The strategic importance of nickel: scenarios and perspectives aimed at global supply," *Trans. Soc. Min., Met. Explor*, vol. 334, pp. 510-518, 2013.

[3] M. Chandrashekar, and K. V. Sreenivasa Prasad, "The effect of cobalt on wear behavior of cemented carbide cutting tools for machining of titanium alloy," *Mater. Today Proc.*, vol. 5, no. 2, pp. 7678-7684, 2018. Doi:10.1016/j.matpr.2017.11.443.

[4] J. M. Costa, M. B. Porto, R. J. Amancio, and A. F. A. Neto, "Effects of tungsten and cobalt concentration on microstructure and anticorrosive property of cobalt-tungsten alloys," *Surfaces and Interfaces*, vol. 20, p. 100626, 2020. Doi:10.1016/j.surfin.2020.100626.

[5] H. A. Zaman, S. Sharif, D. W. Kim, M. H. Idris, M. A. Suhaimi, and Z. Tumurkhuyag, "Machinability of cobalt-based and cobalt chromium molybdenum alloys-a review," *Procedia Manuf.*, vol. 11, pp. 563-570, 2017. Doi: 10.1016/j.promfg.2017.07.150.

[6] E. White, E. Rinko, T. Prost, T. Horn, C. Ledford, C. Rock, and I. Anderson, "Processing of alnico magnets by additive manufacturing," *Appl. Sci.*, vol. 9, no. 22, 2019. Doi:10.3390/app9224843.

[7] C. Demminger, C. Klose, and H. J. Maier, "Microstructure and magnetic properties of cobalt and zinc containing magnesium alloys," *Procedia Technol.*, vol. 26, pp. 35-42, 2016. Doi: 10.1016/j.protcy.2016.08.006.

[8] X. Zhou, A. Huang, B. Cui, and J. W. Sutherland, "Techno-economic assessment of a novel SmCo permanent magnet manufacturing method," *Procedia CIRP*, vol. 98, pp. 127-132, 2021. Doi: 10.1016/j.procir.2021.01.017.

[9] X. Sun, H. Hao, Z. Liu, F. Zhao, and J. Song, "Tracing global cobalt flow: 1995-2015," *Resour. Conserv. Recycl.*, vol. 149, no. April, pp. 45-55, 2019. Doi: 10.1016/j.resconrec.2019.05.009.

[10] A. C. Ghogia, A. Nzihou, P. Serp, K. Soulantica, and D. Pham Minh, "Cobalt catalysts on carbon-based materials for fischer-tropsch synthesis: a review," *Applied Catalysis A: General*, vol. 609, no. 117906, 2021. Doi: 10.1016/j.apcata.2020.117906.

[11] B. Tian, S. Mao, F. Guo, J. Bai, R. Shu, L. Qian, and Q. Liu, "Monolithic biochar-supported cobalt-based catalysts with high-activity and superior-stability for biomass tar reforming," *Energy*, vol. 242, pp. 122970, 2022. Doi: 10.1016/j.energy.2021.122970.

[12] A. C. M. Silva, M. C. D. Silva, P. K. Rohatgi, and R. A. Renzetti, "Cobalt (II)

used as a catalyst to drying properties of healing agents for self-healing coatings," *Brazilian J. Dev.*, vol. 8, no. 2, pp. 9723-9740, 2022. Doi: 10.34117/bjdv8n2-085.

[13] F. J. Anaissi, D. F. L. Horsth, J. Dalastra, J. O. Primo, K. W. Borth, M. L. M. Rocha, and N. Balaba, "Design, synthesis, and application of colored cobalt pigments (pink, blue, green)," *J. Braz. Chem. Soc.*, vol. 31, no. 11, pp. 2265-2273, 2020. Doi:10.21577/0103-5053.20200078.

[14] A. Campanile, B. Liguori, O. Marino, G. Cavaliere, V. L. De Bartolomeis, and D. Caputo, "Facile synthesis of nanostructured cobalt pigments by Co- A zeolite thermal conversion and its application in porcelain manufacture," *Sci. Rep.*, vol. 10, no. 1, pp. 1-9, 2020. Doi:10.1038/s41598-020-67282-1.

[15] G. S. Seck, E. Hache, and C. Barnet, "Potential bottleneck in the energy transition: The case of cobalt in an accelerating electro-mobility world," *Resour. Policy*, vol. 75, pp. 1-4, 2022. Doi:10.1016/j.resourpol.2021.102516.

[16] R. V. Kumar, and A. P. Khandale, "A review on recent progress and selection of cobalt-based cathode materials for low temperature-solid oxide fuel cells," *Renew. Sustain. Energy Rev.*, vol. 156, pp. 111985, 2022. Doi:10.1016/j.rser.2021.111985.

[17] A. Aherwar, A. K. Singh, and A. Patnaik, "Cobalt based alloy: A better choice biomaterial for hip implants," *Trends Biomater. Artif. Organs*, vol. 30, no. 1, pp. 50-55, 2016. Doi: 10.13140/RG.2.1.2501.5284.

[18] K. Kulcsár, and J. Kónya, "The influence of heat treatment on the mechanical properties of 3D-printed cobalt-chrome alloy used in dental laboratory practice," *Acta Mater. Transilv.*, vol. 1, no. 2, pp. 97-100, 2019. Doi:10.2478/amt-2018-0036.

[19] G. Herranz, C. Berges, J. A. Naranjo, C. García, and I. Garrido, "Mechanical performance, corrosion and tribological evaluation of a Co-Cr-Mo alloy processed by MIM for biomedical applications," *J. Mech. Behav. Biomed. Mater.*, vol. 105, pp. 103706, 2020. Doi: 10.1016/j.jmbbm.2020.103706.

[20] A. Shokrani, V. Dhokia, and S. T. Newman, "Cryogenic high speed machining of cobalt chromium alloy," *Procedia CIRP*, vol. 46, pp. 404-407, 2016. Doi:10.1016/j.procir.2016.04.045.

[21] G. Manivasagam, D. Dhinasekaran, and A. Rajamanickam, "Biomedical implants: Corrosion and its prevention - A review," *Recent Patents Corros. Sci.*, vol. 2, no. 1, pp. 40-54, 2010. Doi:10.2174/1877610801002010040.

[22] F. K. Crundwell, N. B. Preez, and B. D. H. Knights, "Production of cobalt from copper-cobalt ores on the african copperbelt-an overview," *Miner. Eng.*, vol. 156, pp. 106450, 2020. Doi: 10.1016/j.mineng.2020.106450.

[23] P. A. Dias, D. Blagoeva, C. Pavel, and N. Arvanitidis, "Cobalt: demand-supply balances in the transition to electric mobility," *JRC Publication Repository,* 2018. Doi:10.2760/97710.

[24] Q. Dehaine, L. T. Tijsseling, H. J. Glass, T. Törmänen, and A. R. Butcher, "Geometallurgy of cobalt ores: A review," *Miner. Eng.*, vol. 160, 2021. Doi: 10.1016/j.mineng.2020.106656.

[25] N. Mulaudzi, and M. H. Kotze, "Direct cobalt electrowinning as an alternative to intermediate cobalt mixed hydroxide product," in *The Southern African Institute of Mining and Metallurgy Base Metals Conference*, pp. 209-222, 2013.

[26] K. G. Fisher, "Cobalt processing developments," in *The Southern African Institute of Mining and Metallurgy 6th Southern African Base Metals Conference*, pp. 237-258, 2011.

[27] K. A. Karimov, A. V. Kritskii, L. G. Elfimova, and S. S. Naboichenko, "Low-temperature pressure leaching of converter matte in sulfuric acid solutions," *Metallurgist*, vol. 61, no. 3-4, pp. 238-242, 2017. Doi:10.1007/s11015-017-0483-z.

[28] Y. Huang, Z. Zhang, Y. Cao, G. Han, W. Peng, X. Zhu, T. Zhang and Z. Dou, "Overview of cobalt resources and comprehensive analysis of cobalt recovery from zinc plant purification residue-a review," *Hydrometallurgy*, vol. 193, p. 105327, 2020. Doi: 10.1016/j.hydromet.2020.105327.

[29] S. S. Afolabi, M. O. Zakariyah, M. H. Abedi, and W. Shafik, "A survey on cobalt metallurgical processes and its application," *J. Indian Chem. Soc.*, vol. 98, no. 11, 2021. Doi: 10.1016/j.jics.2021.100179.

[30] J. Cheng, T. Lu, X. Wu, H. Zhang, C. Zhang, C. Peng, and S. Huang, "Extraction of cobalt(ii) by

methyltrioctylammonium chloride in nickel(ii)-containing chloride solution from spent lithium ion batteries," *RSC Adv.*, vol. 9, no. 39, pp. 22729-22739, 2019. Doi:10.1039/c9ra02719j.

[31] L. Brückner, J. Frank, and T. Elwert, "Industrial recycling of lithium-ion batteries-A critical review of metallurgical process routes," *Metals (Basel).*, vol. 10, no. 8, pp. 1-29, 2020. Doi: 10.3390/met10081107.

[32] R. Subagja, "Nickel extraction from nickel matte," *IOP Conf. Ser. Mater. Sci. Eng.*, vol. 285, no. 1, 2018. Doi: 10.1088/1757-899X/285/1/012001.

[33] M. H. Morcali, L. T. Khajavi, S. Aktas, and D. B. Dreisinger, "Oxidative dissolution of nickel matte in dilute sulfuric acid solutions," *Hydrometallurgy*, vol. 185, pp. 257-265, 2019. Doi: 10.1016/j.hydromet.2019.03.010.

[34] R. Subagja, I. Setiawan, A. R. Rhamdani, and J. Irawan, "Effect of technological parameters on the electrowinning of cobalt from cobalt(II) chloride solutions," *Int. J. Electrochem. Sci.*, vol. 17, pp. 1-18, 2022. Doi:10.20964/2022.09.66.

[35] B. Swain, H. W. Shim, and C. G. Lee, "Extraction/separations of cobalt by supported liquid membrane: A review," *Korean Chem. Eng. Res.*, vol. 57, no. 3, pp. 313-320, 2019. Doi: 10.9713/kcer.2019.57.3.313.

[36] V. I. Francesco, and Veglio, "Separation of manganese, zinc and nickel from leaching solution of nickel-metal hydride spent batteries by solvent extraction", *Hydrometallurgy*, vol. 129-130, pp. 50-58, 2012.

[37] R. Subagja, "Pemisahan ion kobal dari larutan nikel klorida dengan cara solvent ekstraksi", *Teknologi Indonesia*, vol. 34, no. 2, pp. 102-110, 2011.

[38] J. Wang, J. Fu, F. Yu, W. Xu, and H. Wang**,** **"**An efficient extractant (2-ethylhexyl) (2,4,4′-rimethylpentyl) phosphinic acid (USTB-1) for cobalt and nickel separation from sulfate solutions," *Separation and Purification Technology*, vol. 248, 117060, 2020**.** Doi: 10.1016/j.seppur.2020.117060.

[39] L. E. O. C. Rodrigues, and M. B. Mansur, "Hydrometallurgical separation of rare earth elements, cobalt and nickel from spent nickel–metal–hydride batteries," *Journal of Power Sources*, vol. 195, no. 11, pp. 3735-3741, 2010. Doi:10.1016/j.jpowsour.2009.12.071

[40] A. E. Zarandi, D. Azizi, P. A. Nikolaychuk, F. Larachi, and L. C. Pasquier, "Selective recovery of molybdenum over rhenium from molybdenite flue dust leaching solution using PC-88A extractant, " *Metals*, vol.10, no. 1423, 2020. Doi:10.3390/met10111423.

[41] L. Lin, W. J. Hong, W. G. Yi, F. Toyohisa, and S. Atsushi, "Extraction study of cobalt (II) and nickel (II) from chloride solution using PC88A," *Transaction of Metal Society of China*, vol. 16, no. 3, pp. 687-692, 2006. Doi:10.1016/S1003-6326(06)60122-2.

AUTHOR INDEX

SUBJECT INDEX